Legionella pneumophila Modulates Mitochondrial Dynamics to Trigger Metabolic Repurposing of Infected Macrophages

Pedro Escoll, Ok-Ryul Song, Flávia Viana, Bernhard Steiner, Thibault Lagache, Jean-Christophe Olivo-Marin, Francis Impens, Priscille Brodin, Hubert Hilbi, Carmen Buchrieser

Legionella pneumophila modulates mitochondrial dynamics to trigger metabolic repurposing of infected macrophages

Pedro Escoll[1,2], Ok-Ryul Song[3], Flávia Viana[1,2,10], Bernhard Steiner[4,10], Thibault Lagache[5,6], Jean-Christophe Olivo-Marin[5], Francis Impens[7,8,9], Priscille Brodin[3], Hubert Hilbi[4] & Carmen Buchrieser[1,2, 11*]

[1]Institut Pasteur, Biologie des Bactéries Intracellulaires and [2]CNRS UMR 3525, Paris, France, [3]Univ. Lille, CNRS, Inserm, CHU Lille, Institut Pasteur de Lille, U1019 – UMR 8204-CIIL-Center for Infection and Immunity of Lille, F-59000 Lille, France, [4]Institute of Medical Microbiology, University of Zurich, Switzerland, [5]Institut Pasteur, Unité d'Analyse d'Images Biologiques, CNRS UMR 3691, Paris, France, [6]Present address: Department of Biological Sciences, Columbia University, 10027 New-York, [7]VIB-UGent Center for Medical Biotechnology, and [8]VIB Proteomics Core and [9]Department of Biochemistry, Ghent University, 9000 Ghent, Belgium[10] These authors contributed equally, [11]Lead contact

*For correspondence and lead contact:

Carmen Buchrieser

Institut Pasteur, Biologie des Bactéries Intracellulaires

75724 Paris, France

E-mail: ***cbuch@pasteur.fr***

SUMMARY

The intracellular bacteria *Legionella pneumophila* encodes a type IV secretion system (T4SS) that injects effector proteins into macrophages in order to establish and replicate within the *Legionella*-containing vacuole (LCV). Once generated, the LCV interacts with mitochondria through unclear mechanisms. We show that *Legionella* uses both T4SS-independent and T4SS-dependent mechanisms to respectively interact with mitochondria and induce mitochondrial fragmentation that ultimately alters mitochondrial metabolism. The T4SS effector MitF, a Ran GTPase activator, is required for fission of the mitochondrial network. These effects of MitF occur through accumulation of mitochondrial DNM1L, a GTPase critical for fission. Furthermore mitochondrial respiration is abruptly halted in a T4SS-dependent manner, while T4SS-independent upregulation of cellular glycolysis remains elevated. Collectively, these alterations in mitochondrial dynamics promote a Warburg-like phenotype in macrophages that favours bacterial replication. Hence the rewiring of cellular bioenergetics to create a replication permissive niche in host cells is a virulence strategy of *L. pneumophila*.

INTRODUCTION

Macrophages are a first line host defence against bacterial pathogens. Key determinants for their activation and subsequent responses are metabolic changes as shown recently (O'Neill and Pearce, 2016). Important organelles that refine the metabolism of macrophages are mitochondria as critical players in the cellular metabolism and bioenergetics (O'Neill and Pearce, 2016). Moreover, mitochondria have functions in the regulation of cell death and innate immunity (West et al., 2011b). Mitochondrial functions are strongly influenced by the highly dynamic nature of the organelle including organelle localization, morphology, quantity and activity(Labbe et al., 2014). These dynamics are tightly regulated at the single-organelle level to respond to the specific demands of the cell. Whereas localization of mitochondria to specific subcellular positions depends on the mitochondrial Rho GTPases RHOT1/2 (also known as Miro1/2), changes in mitochondrial morphology from elongated networks to single rod-shaped mitochondria, and *vice versa*, are governed by GTPases of the dynamin family such as Mitofusin-1/2, OPA1 and dynamin 1-like protein (DNM1L, also known as DRP1), which are key proteins regulating mitochondrial morphology (Labbe et al., 2014).

Considering the important functions of mitochondria, intracellular bacteria have evolved mechanisms to target these organelles during infection to exploit the key roles they play in the cell (Escoll et al., 2016). One way to subvert mitochondrial functions is to target mitochondrial dynamics. Indeed, it has been shown that the bacterial effector VopE of *Vibrio cholera*e modifies the subcellular localization of mitochondria by interacting with RHOT1/2 proteins (Suzuki et al., 2014) while secretion of the *Listeria monocytogenes* toxin listeriolysin O (LLO) during infection induces fragmentation of mitochondrial networks independently of DNM1L, a key component of the mitochondrial fission machinery (Stavru et al., 2011; Stavru et al., 2013). As mitochondrial dynamics impact mitochondrial bioenergetics and *vice versa*, it is expected that this functional crosstalk also operates during infection. However, the interplay of both processes during bacterial infection remains largely unexplored.

Legionella pneumophila is a Gram-negative, intracellular bacterium and the etiologic agent of Legionnaires' disease, a serious pulmonary infection during which the pathogen replicates within human lung macrophages. *L. pneumophila* encodes a type IV secretion system (T4SS), that injects more than 300 bacterial proteins in the host cytoplasm to subvert multiple host functions to ensure intracellular bacterial replication (Isberg et al., 2009). These different effectors have been shown to target different signalling pathways and host organelles, like

RomA that induces epigenetic regulations in the nucleus (Rolando et al., 2013) or Lp*Spl* and RavZ that target autophagy in the host cell (Choy et al., 2012; Rolando et al., 2016). However, no effector that targets mitochondrial dynamics has been identified yet, although it was reported that the *Legionella*-containing vacuole (LCV) associates with mitochondria. As early as in 1983 it was reported that within 3 min of phagocytosis 30% of vacuoles were surrounded by mitochondria closely apposed to the vacuolar membrane and that at 1h, an even higher proportion of the LCV was surrounded by mitochondria (Horwitz, 1983). Since this observation, it was reported in textbooks and reviews that depended on the T4SS *L. pneumophila* recruits mitochondria or that mitochondria associate with the LCV. However, this phenomenon has never been explored quantitatively, the bacterial T4SS effectors implicated in mitochondrial recruitment have not been identified nor have the mitochondrial functions probably modulated by *L. pneumophila* been elucidated.

Here we used high-content analyses of dynamic fluorescence imaging, at the single-cell level and metabolic assays to reveal mitochondrial responses linked to infection. We performed our study in human primary macrophages infected either with virulent or with non-virulent (T4SS deficient) *L. pneumophila* strains. We revealed that T4SS-dependent and T4SS-independent alterations of mitochondrial dynamics and metabolic responses of infected macrophages occur as early as 6h post-infection and prior to bacterial replication. We show that by targeting mitochondrial dynamics in a T4SS- and DNM1L-dependent manner, *L. pneumophila* induces metabolic repurposing of macrophages and provokes a T4SS-induced Warburg-like effect in the infected macrophages that favours bacterial replication.

RESULTS

L. pneumophila induces highly dynamic mitochondria-phagosome interactions

The proximity of mitochondria with the LCV during *Legionella* infection was first observed using electron microscopy on fixed samples of infected human monocytes (Horwitz, 1983) and shortly after also reported in *Legionella*-infected amoeba, its natural hosts (Newsome et al., 1985). However, observations of this phenomenon in living cells have been scarce if any. We thus infected primary human monocyte-derived macrophages (hMDMs) using GFP-expressing *L. pneumophila* strain Philadelphia JR32 (JR32-WT-GFP), and monitored mitochondrial recruitment to the LCV by time-lapse confocal microscopy in over 600 infected, living cells, using automatic image analysis at the single-cell level (Figure 1A). As it was reported that mitochondrial recruitment to the LCV occurs at early times post infection (p.i.), peaking at 2h p.i. (Horwitz, 1983), we performed the time-lapse experiments up to 6h. At any early time point (from 1 to 6h p.i.), more than 80% of the infected cells had at least 1 mitochondrion in close proximity (<1 μm) of the LCV, with an average of 2.02±0.05 mitochondria per LCV (Figure 1B) confirming early observations using fixed cells. When hMDMs were infected with GFP-expressing *L. pneumophila* strain Paris (Lpp-WT-GFP), we obtained similar results, suggesting that interactions of mitochondria with the LCV are a common feature of *L. pneumophila* (Figure 1C). It was reported that mitochondrial recruitment was T4SS depended (Tilney et al., 2001). We therefore monitored mitochondrial association with the LCV during the infection of hMDMs with T4SS-deficient *L. pneumophila* mutants (JR32-Δ*icmT*-GFP and Lpp-Δ*dotA*-GFP). No differences were observed when comparing JR32-Δ*icmT*-GFP and Lpp-Δ*dotA*-GFP mutants to the wild-type (WT) strains (Figure 1B and 1C), suggesting that mitochondria surround the LCV in a T4SS-independent manner.

To determine the frequency of these interactions we performed 3D confocal time-lapse experiments and recorded the contacts of mitochondria with one LCV over time. Time-lapse confocal 3D reconstructed movies showed that mitochondria-LCV contacts were highly dynamic as these organelles moved to the LCVs, contacted them, tethered during variable but short times, and abandoned the contact with the LCV (Figure 1D and S1, and Movie S1, S2 and S3). To assess whether these dynamic mitochondria-LCV contacts were statistically significantly different as compared to contacts by chance, we developed a statistical method for quantitative 3D image analysis (detailed in *STAR Methods*). As shown in Figure 1E, this

revealed that contacts between mitochondria and the LCV occurred in a highly dynamic manner during the first 4h p.i. Quantification of the frequency of mitochondria-LCV contacts, showed that they occurred with a frequency of 0.90±0.32 contacts/min per LCV when hMDMs were infected with WT and with a frequency of 0.55±0.38 contacts/min per LCV when hMDMs were infected with the Δ*icmT* mutant (Figure 1F). We further compared the frequency of mitochondria-LCV contacts during infection with the frequency of contacts of micro-bead containing phagosomes. As shown in Figure 1F and Movie S4 these contacts occurred in a frequency of 0.73±0.61 contacts/min per LCV, similar to those of the LVC containing WT or Δ*icmT* mutant strains. Although a biological trend can be observed, no significant differences were measured in the frequency of mitochondria-LCV contacts during infection with virulent or avirulent *L. pneumophila* strains or beads, suggesting that these highly dynamic contacts mainly occur independently of the *L. pneumophila* T4SS. A transfer of Mitotracker dye from mitochondria to the LCV occurred occasionally during these dynamic contacts (Figure S2 and Movie S5). Due to the bacterial membrane potential, MitoTracker dyes will most likely also stain *L. pneumophila.* Thus our observation might indicate that after contacts with mitochondria changes in the *L. pneumophila* membrane potential occur. However, as Mitotracker dyes form a covalent bond with thiols on mitochondrial proteins (Cottet-Rousselle et al., 2011), these transient but close couplings might also suggest a transfer of proteins from mitochondria to the LCV. Indeed, 24.9% of the proteins found in the proteome of isolated LCVs from macrophages were mitochondrial proteins (Hoffmann et al., 2014).

Our results thus indicate that instead of recruiting mitochondria, *L. pneumophila* interacts with host mitochondria in a highly dynamic, transient and mainly T4SS-independent manner.

L. pneumophila induces T4SS-dependent changes in mitochondrial morphology during infection

During physiological conditions, mitochondria perform cycles of fission and fusion that affect overall organelle morphology from an elongated mitochondrial network to a fragmented network of single rod-shaped mitochondria (Labbe et al., 2014). To analyse mitochondrial morphology during *L. pneumophila* infection of hMDMs and to uncover whether the T4SS governs mitochondrial dynamics, we performed time-course experiments and single-cell analyses of the mitochondrial morphology in living macrophages infected with GFP-expressing virulent and T4SS deficient *L. pneumophila* strains (Figure 2A and 2B). Reticular

(elongated) or punctuate (fragmented) mitochondria were determined in a high number of infected hMDMs by analysing the images obtained with texture algorithms (Figure 2A and Figure S3) and classical measurements of mitochondrial morphology based on segmentation strategies (Figure S3D). These quantitative, high-content analyses showed that *L. pneumophila* induced mitochondrial fragmentation during the first 6h p.i in a time- and T4SS-dependent manner (Figure 2B), but no alteration of the overall mitochondrial content was observed (Figure S3E). At 6h p.i, macrophages infected with WT strains showed an increased percentage of infected cells with fragmented mitochondria (JR32-WT: 35.53±6.27% and Lpp-WT: 76.64±4.33%) as compared to the avirulent T4SS-deficient mutants (JR32-Δ*icmT*: 8.07±5.39% and Lpp-*ΔdotA*: 36.94±2.66%). Furthermore, *L. pneumophila*-induced mitochondrial fission was completely restored at 4h p.i. upon complementation of the Δ*icmT* mutant (JR32-Δ*icmT*::*icmT*, Figure 2C), suggesting the participation of T4SS translocated effectors in the induction of mitochondrial fragmentation.

Taken together, *L. pneumophila* modifies the morphology of mitochondria in infected macrophages dependent on its T4SS, suggesting that T4SS secreted effectors are involved in *L. pneumophila*-induced mitochondrial fragmentation.

The T4SS effector MitF is involved in *L. pneumophila*-induced fragmentation of mitochondria during infection

To identify the effector(s) involved in mitochondrial fragmentation we infected hMDMs with different, *L. pneumophila* mutants that lacked specific T4SS effectors. As mitochondrial dynamics are known to be governed by cellular GTPases (Chan, 2012) we first chose RalF and LegG1 (Lpg1976) as both are known to target host GTPases. Whereas a mutant lacking the T4SS effector RalF (targets ARF1-GTPase) induced mitochondrial fragmentation like the WT strain, a mutant lacking LegG1 (targets Ran-GTPase) showed a significantly reduced ability to fragment the mitochondrial network in hMDMs compared to the WT (Figure 2D). Complementation of Δ*legG1* with the *legG1* gene restored the fragmentation phenotype (Figure 2E and 2F), confirming the specific participation of LegG1 in the fragmentation process. Furthermore, single cell texture analysis of mitochondria during infection showed that overexpression of *legG1* in the complemented strain caused even stronger mitochondrial fragmentation than the WT strain (Figure 2G). According to its function we named this effector mitochondrial fragmentation factor, MitF. Thus the T4SS effector MitF promotes mitochondrial fragmentation during *L. pneumophila* infection of human macrophages.

L. pneumophila-induced fragmentation depends on DNM1L

Mitochondrial fusion and fission are processes that are highly regulated in eukaryotic cells. The human protein DNM1L, a large GTPase of the dynamin family, is a critical player in the process of mitochondrial fission (Chan, 2012). We thus analysed the recruitment of DNM1L to mitochondria of hMDMs infected with the WT or a Δ*icmT* mutant by measuring the number of DNM1L puncta per μm^2 of host mitochondria (Figure 3A and S4). The number of DNM1L puncta on mitochondria was significantly lower in non infected than in WT infected hMDMs (Figure 3B), suggesting an increased recruitment of DNM1L to host mitochondria during *L. pneumophila* infection. Importantly, Δ*icmT*-infected macrophages showed a significantly reduced number of DNM1L puncta as compared to non-infected or WT-infected macrophages. Thus, the recruitment of DNM1L to host mitochondria coincides with the T4SS-induced fragmentation of mitochondria during *L. pneumophila* infection. Analyses of DNM1L protein levels and its phosphorylation status showed that DNM1L levels are downregulated during infection with the Δ*icmT* mutant, but remained constant during WT infection (up to 6h, Figure 3C). Furthermore, activation of DNM1L by the WT seems related to phosphorylation of Ser616, as it is reduced during infection with the Δ*icmT* mutant but phosphorylation/dephosphorylation of Ser637 seems not affected by neither WT nor Δ*icmT* mutant infection (Figure 3C).

To further substantiate this finding we used Mdivi1, a compound specifically inhibiting DNM1L functions during mitochondrial fission (Cassidy-Stone et al., 2008). When Mdivi1-pretreated hMDMs were infected with the WT, no differences in the percentage of infected cells compared to non-pretreated hMDMs were observed, indicating that uptake of *L. pneumophila* by hMDMs is not affected by Mdivi1 pre-treatment (Figure 3D). However, the percentage of infected cells showing a fragmented phenotype was significantly (p-value=0.023) reduced from 23.26±9.48% in the absence of Mdivi1-pretreatment to 9.74±5.09% in Mdivi1-pretreated, infected hMDMs (Figure 3E). Moreover, silencing of DNM1L with siRNA in RAW264.7 macrophages significantly reduced mitochondrial fragmentation (p-value<0.0001) compared to cells transfected with scramble siRNA (Figure 3F, 3G and S4). To ascertain that Mdivi1 has no adverse effects on *L. pneumophila* we monitored bacterial growth in BYE with Mdivi1 treated or non-treated cell lysates, confirming that the DNM1L inhibitor did not affect bacterial growth (Figure S5). As Mdivi1 only partially abolished the *L. pneumophila* induced fragmentation phenotype, additional factors might be implicated in this process. Thus we used siRNAs to silence also Ran GTPase,

a host target of MitF (LegG1). Indeed, mitochondrial fragmentation was also reduced in RAW264.7 macrophages compared to cells transfected with scramble siRNA (p-value<0.0001). Silencing of the Ran binding protein 2 (RanBP2) also lead to statistical significantly reduced fragmentation (p-value<0.0001) (Figure 3F, 3G and S4). Collectively, our results show that DNM1L has an important role in *L. pneumophila*-induced mitochondrial fragmentation and that Ran and RanBP2 are involved in this process.

Chemical inhibition of DNM1L by pre-treating hMDMs with Mdivi1 reduced intracellular replication of *L. pneumophila* to 35.45% as compared to replication in non-treated hMDMs (Figure 3H and S4), indicating that DNM1L functions are necessary for its optimal intracellular replication. Furthermore, when DNM1L or RanBP2 were silenced in A549 cells (a cell type that also support mitochondrial fragmentation upon *Legionella* infection, Figure S4), intracellular replication of *L. pneumophila* was reduced by 58.66% and 37.33%, respectively, as compared to cells treated with scramble siRNA (Figures 3I and S4), further supporting that DNM1L and RanBP2 favour bacterial replication.

Quantitative proteomics of proteins pulled down with DNM1L antibodies from hMDMs at 6h p.i with either the WT or the Δ*icmT* mutant (triplicates of independent infections of each strain) identified the DNM1L-interacting proteome during infection. Statistical analysis showed that Wiskott-Aldrich Syndrome protein (WASP) interacts with DNM1L (p-value<0.05) during WT-infection of hMDMs, but not during infection with the Δ*icmT* mutant (Figure 3J). Interaction with Arp2/3 complex subunit 5 (ARPC5) was non-significant, but followed the same trend. Interestingly, the WASP and Arp2/3 complex are part of the cellular machinery of actin nucleation and recent studies suggested that actin assembly is needed for DNM1L-mediated mitochondrial fragmentation (Hatch et al., 2016; Li et al., 2015; Moore et al., 2016).

Collectively, our results show that *L. pneumophila*-induced fragmentation of mitochondria depends on the activity of DNM1L that is required for optimal bacterial replication within host cells and that Ran GTPase is also involved in this process, probably related to the regulation of cytoskeletal dynamics.

Despite mitochondrial fragmentation, *L. pneumophila*-infected human macrophages exhibit a lack of cell death signs

Mitochondrial fragmentation and elongation are physiological and dynamic states of the organelle that may be altered during disease (Labbe et al., 2014). Fragmentation of mitochondria is considered as a hallmark of cell death although it remains unclear if it is

essential for cell death activation (James and Martinou, 2008). However, cell death of macrophages seems to be a defence mechanism against pathogens (Chow et al., 2016). To analyse whether cell death is induced by *L. pneumophila* at this stage of the infection, we measured absolute numbers of total cells and percentage of apoptotic nuclei of WT-infected hMDMs as compared to non-infected cells. Interestingly, at 6h p.i., similar numbers of apoptotic cells were observed in infected and non-infected cells. As expected, macrophages exposed to the pro-apoptotic compound Staurosporin showed high numbers of apoptotic cells (Figure 4A). This suggests that, if signalling leading to cell death was started at this time of infection, it could only be a very early event in the pathway leading to cell death.

As release of Cytochrome C (CytC) from mitochondria is a signal leading to cell death, we imaged CytC in WT and Δ*icmT*-infected hMDMs. CytC remained in the mitochondria at 6h p.i. (Figure 4B) and, interestingly, even until 12h p.i., when *L. pneumophila* has already completed several rounds of replication (Figure 4C). This finding was confirmed by quantifying the mean fluorescence intensity of CytC in mitochondria (Figure 4D) and by analysing CytC quantity by fractionation and western blot (Figure 4E). Thus *L. pneumophila*-induced mitochondrial fragmentation does not trigger the release of CytC and cell death pathways are not activated at the time where mitochondrial fragmentation can be seen in WT-infected cells (6h p.i. Figure 2). We then stained living hMDMs with AnnexinV, a well-known marker of early cell death, and quantified the percentage of AnnexinV$^+$ macrophages during infection by flow cytometry. At 6h p.i. only 4.2% of WT-infected cells were AnnexinV$^+$ further supporting our results (Figure 4F). We then monitored Caspase-1 activation at 6h p.i. but did not detect its activation at this time point by any of the *L. pneumophila* strains (Figure 4G). Similarly, when several Caspases were measured, we found that only 2.3% of WT-infected macrophages had activated caspases (Figure 4H).

Taken together, our results demonstrate that *L. pneumophila*-induced DNM1L-dependent mitochondrial fragmentation is not concurrent with cell death in hMDMs at 6h p.i, as there is a lack of cell death signs. This suggests that mitochondrial fission is an *L. pneumophila*-induced cellular event segregated from cell death pathways.

L. pneumophila **impairs mitochondrial respiration during infection in a T4SS- and DNM1L-dependent manner**

Mitochondrial morphology impacts mitochondrial bioenergetics (Yu et al., 2015). Thus we investigated whether *L. pneumophila* infection modulates mitochondrial respiration. First, we measured the oxygen consumption rate (OCR) in kinetic experiments during infection of

living hMDMs with the WT and the Δ*icmT* mutant. Infection rapidly upregulated mitochondrial respiration peaking at 1h p.i. suggesting that it is T4SS-independent. As infection progressed, oxygen consumption was abruptly decreased in WT-infected hMDMs compared to non-infected cells, while Δ*icmT*-infected hMDMs maintained a high OCR compared to non-infected cells (Figure 5A). We thus propose that a biphasic regulation of mitochondrial respiration during *L. pneumophila* infection takes place, where a T4SS-independent phase of increased oxygen consumption that peaks at 1h p.i. is followed by a later T4SS-dependent phase of impaired mitochondrial respiration with an abrupt reduction in oxygen consumption. To learn whether *L. pneumophila*-induced impairment of mitochondrial respiration depends on DNM1L, we pre-treated hMDMs with Mdivi-1 during 4h prior to infection. Indeed, Mdivi-1 pre-treatment attenuated WT-induced impairment of oxygen consumption (Figure 4A), suggesting that in hMDMs not only T4SS-dependent impairment of mitochondrial morphology but also mitochondrial respiration depends on DNM1L activity.

To gain insight into the respiratory status of mitochondria during *L. pneumophila* infection, we analysed cellular respiration in infected macrophages at 2h or 6h p.i. by adding sequentially Oligomycin, an inhibitor of mitochondrial F_1F_O-ATPase, FCCP, an ionophore that uncouples mitochondrial respiration by increasing H^+ transport across the inner mitochondrial membrane and Rotenone and Antimycin A, inhibitors of mitochondrial complex I and III, respectively to impact mitochondrial oxygen consumption (Figure 5B and S6). At 2h p.i. the basal respiration was higher in Δ*icmT*-infected macrophages compared to non-infected and WT-infected cells (Figure 5B), confirming our previous results (Figure 5A). Addition of Oligomycin at 2h p.i. revealed that Oligomycin-induced reduction of cellular OCR was equivalent in non-infected, WT-infected and Δ*icmT*-infected macrophages, indicating that ATP production was not affected by the WT at this time point. Subsequent addition of FCCP, that stimulates respiration, showed that maximal mitochondrial respiration was higher in Δ*icmT*-infected macrophages than in WT-infected cells, leading in both conditions to higher maximal respiration as compared to non-infected cells. Subsequent addition of Rotenone and Antimycin A showed that non-mitochondrial respiration was slightly higher in both WT- and Δ*icmT*-infected cells as compared to non-infected cells. In macrophages the activity of non-mitochondrial NADPH oxidases may dominate cellular oxygen uptake, however our results indicated that this is not the case during *L. pneumophila* infection.

At 6h p.i. the WT strain has induced the morphological changes in mitochondria (Figure 2A and 2B). At this time-point WT-infected cells showed a reduced slope in the reduction of oxygen consumption caused by the addition of Oligomycin, suggesting that mitochondrial ATP production was compromised in WT-infected macrophages (Figure 5C), a result that was further confirmed by measuring intracellular ATP during infection (Figure 5D). In addition, maximal respiration was severely decreased below the levels of non-infected macrophages, while maximal respiration of Δ*icmT*-infected cells remained high.

In order to confirm the role of the T4SS in the impairment of mitochondrial respiration and mitochondrial ATP production, we measured oxygen consumption of hMDMs at 6h post-infection with the complemented Δ*icmT* mutant (JR32-Δ*icmT*::*icmT*) (Figure 5E) and their intracellular ATP content (Figure 5D). Indeed, the ability to impair respiration and to reduce ATP production was restored. Moreover, when other components of the T4SS, such as *icmP* or *dotA* were deleted, the phenotype was consistent with an increased respiration compared to non-infected cells, while complementation (*ΔicmP*::*icmP*) impaired respiration (Figure 5E) independent of bacterial respiration and ATP (Figure S6). Infection with *L. pneumophila* Paris (Lpp WT) and its avirulent Δ*dotA* mutant yielded analogous results (Figure 5E), showing that respiration impairment is conserved in different *L. pneumophila* strains.

In conclusion, *L. pneumophila* infection induces a biphasic regulation of mitochondrial respiration in hMDMs, with a first phase of a T4SS-independent upregulation of oxygen consumption that is followed by a T4SS-dependent phase where mitochondrial respiration is dramatically decreased, mitochondrial ATP production is impaired and the cellular ATP pool is reduced. DNM1L activity is involved in this second phase, suggesting that *L. pneumophila*-induced mitochondrial fragmentation impairs oxidative phosphorylation during infection.

L. pneumophila induces glycolysis during infection in a T4SS-independent manner

As glycolysis is an alternative pathway to produce ATP in the cell when mitochondrial respiration is compromised, we measured the extracellular acidification rate (ECAR) during *L. pneumophila* infection as an output of cellular glycolysis. Figure 5F shows that macrophages infected with WT or Δ*icmT* upregulated glycolysis 1h p.i.. Next, we pre-treated hMDMs with 2-deoxi-glucose (2-DG), an inhibitor of glycolysis, or with Oligomycin, an inhibitor of mitochondrial F_1F_O-ATPase. Whereas 2-DG pre-treatment reduced intracellular replication of the WT strain significantly to 46.03±11.45% (p-value=0.0036), Oligomycin pre-treatment had no significant effect (Figure 5G and S5), highlighting the importance of

host cell glycolysis for optimal intracellular replication of *L. pneumophila* early in infection, while mitochondrial oxidative phosphorylation seems dispensable. Thus, our data suggest that *L. pneumophila* infection upregulates cellular glycolysis independently of the T4SS, and that a functional glycolysis is required for optimal intracellular replication in human macrophages, while mitochondrial ATP production seems largely dispensable.

DISCUSSION

Although it was reported over 30 years ago (Horwitz, 1983) that mitochondria associate with the bacterial vacuole, the functions of such an association and a possible effector implicated remained unknown. Here we show that *L. pneumophila* regulates mitochondrial dynamics to subvert mitochondrial bioenergetics of infected cells in a process that involves the bacterial T4SS effector MitF and the host fission protein DNM1L. Surprisingly, *L. pneumophila* induced mitochondrial fragmentation is independent of cell death and ultimately impairs mitochondrial respiration, whereas cellular glycolysis is increased. Thus *L. pneumophila* infection of hMDMs induces changes in mitochondrial dynamics that promote a Warburg-like phenotype in the infected cell that favours bacterial replication.

Contrary to what was reported before, live cell imaging of mitochondria during infection of hMDMs revealed that *L. pneumophila* does not recruit mitochondria to the LCV, but it interacts with host mitochondria in a highly dynamic manner through close and transient couplings independently of T4SS effectors (Figure 1). We quantified the dynamics of the mitochondria-LCV contacts using statistical analysis of 3D time-lapses of single, infected cells. Physical interactions of the phagosome with mitochondria have been reported for *Chlamydia*, *Salmonella* or *Shigella* infections (Hall et al., 2013; Matsumoto et al., 1991; Sirianni et al., 2016) however, comparisons are difficult as these interactions had not been quantified in time-lapse experiments in living cells. Here we demonstrate that, although mitochondria can be nearly always found in close proximity to the LCV during the first 6h p.i., these contacts are highly dynamic, transient and mainly T4SS-independent. The absence of T4SS participation in this process suggests that mitochondria-LCV couplings might be inherent to phagosome formation and processing. Indeed, associations of mitochondria and phagosomes were also observed when macrophages phagocytized LPS-coated latex beads (West et al., 2011a), pointing to an infection-dependent but virulence-independent mechanism. Our quantitative data therefore support a model where *L. pneumophila* induces highly dynamic and transient interactions with mitochondria without the participation of T4SS effectors. Moreover, as mitochondrial fragmentation without alterations in the mitochondrial

mass (Figure S3E) implies an increase in the number of single mitochondria, the probability of mitochondria contacting the LCV might be increased, suggesting that what was reported over 30 years ago might not be recruitment of mitochondria to the LCV but an increase of LCV-mitochondria contacts due to WT-induced mitochondrial fragmentation.

While highly dynamic mitochondria-LCV contacts occur mainly T4SS-independent, our analyses of mitochondrial morphology during infection indicate that translocation of T4SS effectors induces mitochondrial fission in the host cell. We found that the T4SS secreted effector MitF is involved (Figure 2), although participation of other effectors cannot be excluded. MitF is a bacterial activator of host Ran-GTPase that has been shown to modulate cytoskeleton dynamics and cell migration of host cells during infection (Rothmeier et al., 2013; Simon et al., 2014). Here we show that the *L. pneumophila* Δ*mitF* mutant has an impaired ability to fragment host mitochondria, whereas plasmid-borne expression of MitF complements the phenotype and leads to even more dramatic mitochondrial fragmentation than the WT strain, confirming its participation in *L. pneumophila*-induced changes of mitochondrial dynamics in hMDMs. A BLASTP search with Lpg1976/MitF revealed that homologues of MitF are present in 15 *L. pneumophila* strains and in eight out of 41 *Legionella* species analysed, suggesting that also other *L. pneumophila* strains and *Legionella* species induce mitochondrial fragmentation. To our knowledge, to date only the bacterial toxins listeriolysin O (LLO) of *L. monocytogenes* and the vacuolating toxin A (VacA) of *H. pylori* have been implicated in bacterial-induced mitochondrial fragmentation, but no translocated protein has been identified yet (Jain et al., 2011; Stavru et al., 2011). Thus, uniquely, the translocated bacterial effector MitF of *L. pneumophila* promotes mitochondrial fragmentation in the host cell.

On the host side, the fission factor DNM1L aggregates on host mitochondria during *L. pneumophila* infection in a T4SS-dependent manner (Figure 3). Pre-treatment of hMDMs with Mdivi1, an inhibitor of DNM1L functions on mitochondrial fission reduced *L. pneumophila*-induced mitochondrial fragmentation, suggesting a participation of DNM1L in the morphological changes of mitochondria. Furthermore, the host factors Ran and RanBP2 are involved in the fragmentation process. Targeting of DNM1L by Mdivi1 or siRNA-mediated silencing reduced bacterial intracellular replication, suggesting that DNM1L-induced fragmentation is required for optimal intracellular replication of *L. pneumophila*. These results are in line with data obtained for *L. monocytogenes*, where depletion of DNM1L impaired bacterial replication, suggesting that *L. monocytogenes* needs to induce mitochondrial fission for efficient infection (Stavru et al., 2011). However,

L. monocytogenes-induced mitochondrial fragmentation occurs independently of DNM1L (Stavru et al., 2013) different from what we find for *L. pneumophila* and what was reported for *H. pylori* that fragment mitochondria through DNM1L (Jain et al., 2011).

Our quantitative proteomic approach shows that DNM1L specifically interacts with WASP during *L. pneumophila*-WT-infection, while it also suggests that DNM1L interacts with ARPC5, a subunit of the Arp2/3 complex. As WASP and the Arp2/3 complex are known to be involved in actin nucleation in macrophages (Rougerie et al., 2013) and recent studies suggested that actin assembly is needed to recruit DNM1L to the fission site by direct binding (Hatch et al., 2016; Li et al., 2015; Moore et al., 2016), this indicates that *L. pneumophila*-induced mitochondrial fragmentation may involve WASP-Arp2/3-mediated recruitment of DNM1L to mitochondria. Moreover, the effector MitF (LegG1) for which we have shown here involvement in *L. pneumophila*-induced mitochondrial fragmentation (Figure 3) is an activator of cellular Ran which targets RanBP2 (Rothmeier et al., 2013). Importantly, it has been shown that Ran regulates WASP and Arp2/3 for actin nucleation (Yi et al., 2011), and both Ran and RanBP2 have been found to directly interact with WASP (Sadhukhan et al., 2014). Thus, cytoskeletal dynamics might – at least partly – account for MitF functions on mitochondrial fragmentation during *L. pneumophila* infection through a Ran – RanBP2 – WASP/Arp2/3 – DNM1L functional axe.

It has been proposed that DNM1L participates in apoptotic cell death by stimulating Bax oligomerization and thereby enhancing MOM permeabilization and massive efflux of Cytochrome C (Montessuit et al., 2010). Our data support a model where during *L. pneumophila* infection DNM1L functions in mitochondrial dynamics and cell death pathways are segregated, as we observed an increase of DNM1L puncta on mitochondria in the absence of early or late signs of cell death in the infected cells, including Cytochrome C release or Caspase activation. Indeed, these two functions seem to be intrinsically separated in the DNM1L protein, as DNM1L-induced mitochondrial fission relies on its GTPase activity while DNM1L-induced Bax oligomerization and promotion of cell death appears independent of its GTPase activity (Montessuit et al., 2010). Moreover, Bax oligomerization in mitochondria seems not forcibly dependent on DNM1L, as *dnm1l*$^{-/-}$ cells still recruit Bax and Bak to mitochondria (Otera et al., 2016). This may suggest that the role of DNM1L during *L. pneumophila* infection is restricted to its GTPase activity, whereas its functions on MOM permeabilization, Cytochrome C release and finally cell death are inactive. Importantly, *L. pneumophila* specifically modulates several cell death mediators of macrophages at different levels of the apoptotic cascade (Luo, 2011), which may also interact with DNM1L-

induced signalling. Interestingly, our results show that cell death is not an obligate outcome of disrupting mitochondrial dynamics. In addition, the lack of cell death induction in the infected cell might benefit intracellular *L. pneumophila*, as the niche where bacterial replication takes place is preserved.

A key finding of our study is the discovery that *L. pneumophila*-induced mitochondrial fission alters the bioenergetics of infected macrophages leading to a Warburg-like metabolism in the cells. Induction of glycolysis and initial upregulation of mitochondrial respiration is independent of *L. pneumophila* T4SS effectors, but at 60min p.i. *L. pneumophila* abruptly reduces mitochondrial oxygen consumption, ATP turnover and the intracellular ATP pool by a mechanism dependent on a functional T4SS and involving DNM1L (Figure 5). Our results indicate that *L. pneumophila*-induced DNM1L-mediated mitochondrial fragmentation plays a key role in the regulation of mitochondrial respiration during infection.

We propose that as early as 6h p.i. and prior to bacterial replication, *L. pneumophila*-induced mitochondrial changes allow to repurpose the metabolism of the infected cell in a way where oxidative phosphorylation is impaired while cellular glycolysis remains active. This metabolic switch of the infected host cell strikingly resembles the Warburg effect, a metabolic state observed in a wide range of cancer cells where respiration in mitochondria is limited and glycolysis is enhanced (Liberti and Locasale, 2016). Originally defined in tumor cells, Warburg-like processes are also observed during immune responses and inflammation (Wen et al., 2012). In line with this idea is the fact that intracellular replication of *L. monocytogenes* is favoured in cancer cells as compared to infection of primary cells, suggesting that Warburg metabolism might benefit bacterial replication (Gillmaier et al., 2012). Our experiments show that inhibition of oxidative phosphorylation has little effect on *L. pneumophila* replication, while reduction of cellular glycolysis significantly impairs its replication, in line with previous reports (Ogawa et al., 1994), indicating that *L. pneumophila* takes advantage of this Warburg-like metabolism for its intracellular growth in hMDMs.

Taken together, we propose a model (Figure 6) where *L. pneumophila*, by targeting mitochondrial dynamics, induces metabolic repurposing of macrophages and provokes a T4SS-induced Warburg-like effect in the infected cell thereby favouring its own replication. Thus, our results strongly suggest that the bacteria-induced modulation of the mitochondrial dynamics during infection shapes host metabolic responses and represents a key virulence strategy used by *L. pneumophila* to successfully replicate within human macrophages and cause disease.

AUTHOR CONTRIBUTIONS

PE and CB conceived the study; PE, ORS, FV, BS, FI performed experiments; TL developed data analyses algorithms; PE, ORS, FV, TL, FI analysed the data. JCOM, PB, HH, CB supervised the study and provided critical advice; PE and CB wrote the manuscript.

ACKNOWLEDGEMENTS

Work in CB laboratory is financed by Institut Pasteur and ANR-10-LABX-62-IBEID. FV was funded by ANR-13-IFEC-0003-02 (Infect-ERA project EUGENPATH), PE by FRM project DEQ20120323697. We thank N Aulner, JY Tinevez and the Imagopole-CiTech (part of FranceBioImaging supported by ANR-10-INSB-04-01, Conseil de la Region Ile-de-France, FRM) and the Technology Core of the Center for Translational Science (CRT) at Institut Pasteur, for support in conducting this study. Work in JCOM laboratory was partially funded by a Roux Fellowship (Institut Pasteur) to TL and ANR-10-INBS-04-06 FranceBioImaging and ANR-10-LABX-62-IBEID. HH was supported by the Institute of Medical Microbiology, University of Zürich, the Swiss National Science Foundation (SNF; 31003A_153200), and the German Bundesministerium für Bildung und Forschung (BMBF; 031A410A; Infect-ERA project EUGENPATH). FI is supported by VIB and Odysseus grant G0F8616N from the Research Foundation Flanders (FWO). PB and ORS received financial support from the European Community (ERC-STG INTRACELLTB n° 260901, MM4TB n°260872), the ANR-10-EQPX-04-01 and the Région Nord Pas de Calais (convention n° 12000080). All authors declare no conflicts of interest.

REFERENCES

Cassidy-Stone, A., Chipuk, J.E., Ingerman, E., Song, C., Yoo, C., Kuwana, T., Kurth, M.J., Shaw, J.T., Hinshaw, J.E., Green, D.R., *et al.* (2008). Chemical inhibition of the mitochondrial division dynamin reveals its role in Bax/Bak-dependent mitochondrial outer membrane permeabilization. Dev Cell *14*, 193-204.

Chan, D.C. (2012). Fusion and fission: interlinked processes critical for mitochondrial health. Annu Rev Genet *46*, 265-287.

Chow, S.H., Deo, P., and Naderer, T. (2016). Macrophage cell death in microbial infections. Cell Microbiol *18*, 466-474.

Choy, A., Dancourt, J., Mugo, B., O'Connor, T.J., Isberg, R.R., Melia, T.J., and Roy, C.R. (2012). The *Legionella* effector RavZ inhibits host autophagy through irreversible Atg8 deconjugation. Science *338*, 1072-1076.

Cottet-Rousselle, C., Ronot, X., Leverve, X., and Mayol, J.F. (2011). Cytometric assessment of mitochondria using fluorescent probes. Cytometry A *79*, 405-425.

Cox, J., Hein, M.Y., Luber, C.A., Paron, I., Nagaraj, N., and Mann, M. (2014). Accurate proteome-wide label-free quantification by delayed normalization and maximal peptide ratio extraction, termed MaxLFQ. Mol Cell Proteomics *13*, 2513-2526.

Cox, J., and Mann, M. (2008). MaxQuant enables high peptide identification rates, individualized p.p.b.-range mass accuracies and proteome-wide protein quantification. Nat Biotechnol *26*, 1367-1372.

de Chaumont, F., Dallongeville, S., Chenouard, N., Herve, N., Pop, S., Provoost, T., Meas-Yedid, V., Pankajakshan, P., Lecomte, T., Le Montagner, Y., *et al.* (2012). Icy: an open bioimage informatics platform for extended reproducible research. Nat Methods *9*, 690-696.

Escoll, P., Mondino, S., Rolando, M., and Buchrieser, C. (2016). Targeting of host organelles by pathogenic bacteria: a sophisticated subversion strategy. Nat Rev Microbiol *14*, 5-19.

Gillmaier, N., Gotz, A., Schulz, A., Eisenreich, W., and Goebel, W. (2012). Metabolic responses of primary and transformed cells to intracellular *Listeria monocytogenes*. PLoS One *7*, e52378.

Hall, C.J., Boyle, R.H., Astin, J.W., Flores, M.V., Oehlers, S.H., Sanderson, L.E., Ellett, F., Lieschke, G.J., Crosier, K.E., and Crosier, P.S. (2013). Immunoresponsive gene 1 augments bactericidal activity of macrophage-lineage cells by regulating beta-oxidation-dependent mitochondrial ROS production. Cell Metab *18*, 265-278.

Hatch, A.L., Ji, W.K., Merrill, R.A., Strack, S., and Higgs, H.N. (2016). Actin filaments as dynamic reservoirs for Drp1 recruitment. Mol Biol Cell *27*, 3109-3121.

Hoffmann, C., Finsel, I., Otto, A., Pfaffinger, G., Rothmeier, E., Hecker, M., Becher, D., and Hilbi, H. (2014). Functional analysis of novel Rab GTPases identified in the proteome of purified *Legionella*-containing vacuoles from macrophages. Cell Microbiol *16*, 1034-1052.

Horwitz, M.A. (1983). Formation of a novel phagosome by the Legionnaires' disease bacterium (*Legionella pneumophila*) in human monocytes. J Exp Med *158*, 1319-1331.

Isberg, R.R., O'Connor, T.J., and Heidtman, M. (2009). The *Legionella pneumophila* replication vacuole: making a cosy niche inside host cells. Nat Rev Microbiol *7*, 13-24.

Jain, P., Luo, Z.Q., and Blanke, S.R. (2011). *Helicobacter pylori* vacuolating cytotoxin A (VacA) engages the mitochondrial fission machinery to induce host cell death. Proc Natl Acad Sci U S A *108*, 16032-16037.

James, D.I., and Martinou, J.C. (2008). Mitochondrial dynamics and apoptosis: a painful separation. Dev Cell *15*, 341-343.

Labbe, K., Murley, A., and Nunnari, J. (2014). Determinants and functions of mitochondrial behavior. Annu Rev Cell Dev Biol *30*, 357-391.

Lagache, T., Sauvonnet, N., Danglot, L., and Olivo-Marin, J.C. (2015). Statistical analysis of molecule colocalization in bioimaging. Cytometry A *87*, 568-579.

Li, S., Xu, S., Roelofs, B.A., Boyman, L., Lederer, W.J., Sesaki, H., and Karbowski, M. (2015). Transient assembly of F-actin on the outer mitochondrial membrane contributes to mitochondrial fission. J Cell Biol *208*, 109-123.

Liberti, M.V., and Locasale, J.W. (2016). The Warburg Effect: How Does it Benefit Cancer Cells? Trends Biochem Sci *41*, 211-218.

Luo, Z.Q. (2011). Striking a balance: modulation of host cell death pathways by *Legionella pneumophila*. Front Microbio *2*, doi: 10.3389/fmicb.2011.00036.

Matsumoto, A., Bessho, H., Uehira, K., and Suda, T. (1991). Morphological studies of the association of mitochondria with chlamydial inclusions and the fusion of chlamydial inclusions. J Electron Microsc (Tokyo) *40*, 356-363.

Montessuit, S., Somasekharan, S.P., Terrones, O., Lucken-Ardjomande, S., Herzig, S., Schwarzenbacher, R., Manstein, D.J., Bossy-Wetzel, E., Basanez, G., Meda, P., *et al.*

(2010). Membrane remodeling induced by the dynamin-related protein Drp1 stimulates Bax oligomerization. Cell *142*, 889-901.
Moore, A.S., Wong, Y.C., Simpson, C.L., and Holzbaur, E.L. (2016). Dynamic actin cycling through mitochondrial subpopulations locally regulates the fission-fusion balance within mitochondrial networks. Nature communications *7*, 12886.
Newsome, A.L., Baker, R.L., Miller, R.D., and Arnold, R.R. (1985). Interactions between *Naegleria fowleri* and *Legionella pneumophila*. Infect Immun *50*, 449-452.
O'Neill, L.A., and Pearce, E.J. (2016). Immunometabolism governs dendritic cell and macrophage function. J Exp Med *213*, 15-23.
Ogawa, M., Yoshida, S., and Mizuguchi, Y. (1994). 2-Deoxy-D-glucose inhibits intracellular multiplication and promotes intracellular killing of *Legionella pneumophila* in A/J mouse macrophages. Infect Immun *62*, 266-270.
Olivo-Marin, J.C. (2002). Extraction of spots in biological images using multiscale products. Pattern Recognit *35*, 1989-1996.
Otera, H., Miyata, N., Kuge, O., and Mihara, K. (2016). Drp1-dependent mitochondrial fission via MiD49/51 is essential for apoptotic cristae remodeling. J Cell Biol *212*, 531-544.
Rolando, M., Escoll, P., Nora, T., Botti, J., Boitez, V., Bedia, C., Daniels, C., Abraham, G., Stogios, P.J., Skarina, T., *et al.* (2016). *Legionella pneumophila* S1P-lyase targets host sphingolipid metabolism and restrains autophagy. Proc Natl Acad Sci U S A *113*, 1901-1906.
Rolando, M., Sanulli, S., Rusniok, C., Gomez-Valero, L., Bertholet, C., Sahr, T., Margueron, R., and Buchrieser, C. (2013). *Legionella pneumophila* effector RomA uniquely modifies host chromatin to repress gene expression and promote intracellular bacterial replication. Cell Host Microbe *13*, 395-405.
Rothmeier, E., Pfaffinger, G., Hoffmann, C., Harrison, C.F., Grabmayr, H., Repnik, U., Hannemann, M., Wolke, S., Bausch, A., Griffiths, G., *et al.* (2013). Activation of Ran GTPase by a *Legionella* effector promotes microtubule polymerization, pathogen vacuole motility and infection. PLoS Pathog *9*, e1003598.
Rougerie, P., Miskolci, V., and Cox, D. (2013). Generation of membrane structures during phagocytosis and chemotaxis of macrophages: role and regulation of the actin cytoskeleton. Immunol Rev *256*, 222-239.
Sadhukhan, S., Sarkar, K., Taylor, M., Candotti, F., and Vyas, Y.M. (2014). Nuclear role of WASp in gene transcription is uncoupled from its ARP2/3-dependent cytoplasmic role in actin polymerization. J Immunol *193*, 150-160.
Simon, S., Wagner, M.A., Rothmeier, E., Muller-Taubenberger, A., and Hilbi, H. (2014). Icm/Dot-dependent inhibition of phagocyte migration by *Legionella* is antagonized by a translocated Ran GTPase activator. Cell Microbiol *16*, 977-992.
Sirianni, A., Krokowski, S., Lobato-Marquez, D., Buranyi, S., Pfanzelter, J., Galea, D., Willis, A., Culley, S., Henriques, R., Larrouy-Maumus, G., *et al.* (2016). Mitochondria mediate septin cage assembly to promote autophagy of *Shigella*. EMBO Rep *17*, 1029-1043.
Stavru, F., Bouillaud, F., Sartori, A., Ricquier, D., and Cossart, P. (2011). Listeria monocytogenes transiently alters mitochondrial dynamics during infection. Proc Natl Acad Sci U S A *108*, 3612-3617.
Stavru, F., Palmer, A.E., Wang, C., Youle, R.J., and Cossart, P. (2013). Atypical mitochondrial fission upon bacterial infection. Proc Natl Acad Sci U S A *110*, 16003-16008.
Tilney, L.G., Harb, O.S., Connelly, P.S., Robinson, C.G., and Roy, C.R. (2001). How the parasitic bacterium *Legionella pneumophila* modifies its phagosome and transforms it into rough ER: implications for conversion of plasma membrane to the ER membrane. J Cell Sci *114*, 4637-4650.

643 Wen, H., Ting, J.P., and O'Neill, L.A. (2012). A role for the NLRP3 inflammasome in
644 metabolic diseases--did Warburg miss inflammation? Nat Immunol *13*, 352-357.
645 West, A.P., Brodsky, I.E., Rahner, C., Woo, D.K., Erdjument-Bromage, H., Tempst, P.,
646 Walsh, M.C., Choi, Y., Shadel, G.S., and Ghosh, S. (2011a). TLR signalling augments
647 macrophage bactericidal activity through mitochondrial ROS. Nature *472*, 476-480.
648 West, A.P., Shadel, G.S., and Ghosh, S. (2011b). Mitochondria in innate immune responses.
649 Nat Rev Immunol *11*, 389-402.
650 Yi, K., Unruh, J.R., Deng, M., Slaughter, B.D., Rubinstein, B., and Li, R. (2011). Dynamic
651 maintenance of asymmetric meiotic spindle position through Arp2/3-complex-driven
652 cytoplasmic streaming in mouse oocytes. Nat Cell Biol *13*, 1252-1258.
653 Yu, T., Wang, L., and Yoon, Y. (2015). Morphological control of mitochondrial bioenergetics.
654 Front Biosci (Landmark Ed) *20*, 229-246.
655

FIGURE LEGENDS

Figure 1. *L. pneumophila* establishes transient and highly dynamic contacts with mitochondria of infected human macrophages. (A) Human monocyte-derived macrophages (hMDMs) stained with Mitotracker (red) and Hoechst (cyan) were infected with GFP-expressing *L. pneumophila* (green) and imaged by confocal microscopy each hour and analysed by HCA (mitochondria at <1 μm of the LCV). Scale bar: 5 μm. (**B**) HCA analysis of mitochondria-LCV associations during WT or Δ*icmT* infection of hMDMs. The % of infected cells, the % of LCV with mitochondria at <1 μm and number of mitochondria per LCV are shown (n=3). (**C**) Same as in B but during infection with *L. pneumophila* Paris WT (Lpp-WT) or Lpp-Δ*dotA* (n=3). (**D**) 3D confocal time-lapse images of a WT infected hMDM showing highly dynamic *Legionella*-mitochondria contacts (5 min). Mitochondria (red), *Legionella* (green). Details of the contacts in the inset. See also Figure S1 and Movie S1. (**E**) Quantification of *Legionella*-mitochondria contacts in a whole hMDM cell during 5 h of WT infection. See also Figure S1 and Movies S1 and S2. (**F**) Frequency of quantified *Legionella*-mitochondria contacts during WT or Δ*icmT* infection of hMDMs or phagocytosed microbeads (n=7 cells, ns=non-significant, Mann-Whitney t-test)

Figure 2. *L. pneumophila* induces T4SS-dependent changes in mitochondrial morphology during infection, MitF effector is involved. (**A**) hMDMs stained with Mitotracker (red) and Hoechst (cyan) were infected with GFP-expressing *L. pneumophila* (green), imaged by confocal microscopy each hour and analysed by HCA. High resolution raw images (inset) were filtered and automatically segmented to detect nuclei, cytoplasm and LCVs. SER-Edge and SER-Ridge algorithms for texture analysis were applied to analyse mitochondrial morphology of infected cells. Scale bars: 5 μm. (**B**) HCA analysis of mitochondrial morphology during JR32-WT or JR32-Δ*icmT* infection of hMDMs (upper graph) and Lpp-WT or Lpp-Δ*dotA* (bottom graph) infection. % of infected cells with fragmented mitochondria (n=7). (**C**) HCA analysis of mitochondrial morphology at 4h p.i. with CFSE-labelled JR32-WT, Δ*icmT* or Δ*icmT*-empty vector (JR32-Δ*icmT*::vector) or complemented with *icmT* (*icmT*::*icmT*). % of infected cells with fragmented mitochondria (n=3). (**D**) HCA analysis of mitochondrial morphology (hMDMs) at 4h p.i. with WT, JR32-Δ*icmT*, JR32-Δ*mitF* or JR32-Δ*ralF*. % of infected cells with fragmented mitochondria (n=3). (**E**) RAW264.7 macrophages imaged at 8h p.i. WT, Δ*icmT*, Δ*mitF* or Δ*mitF*::*mitF* (in green).

Cells were stained with Mitotracker Deep Red (red) before fixation. Scale bar: 5 μm. (**F**) % of infected cells with fragmented mitochondria. RAW264.7 macrophages infected with dsRed-expressing WT, Δ*icmT*, Δ*mitF* or complemented strain Δ*mitF*::*mitF* at 8h p.i. (n =2). **(G)** Single-cell results from F are shown. Each dot represents a cell (n > 50 cells per condition). ∗p-value ≤ 0.05; ∗∗p-value ≤ 0.01; ∗∗∗p-value ≤ 0.001; ns = non-significant (Mann-Whitney t-test).

Figure 3. *L. pneumophila*-induced fragmentation depends on DNM1L, necessary for optimal bacterial replication. (A) hMDMs infected with GFP-expressing *L. pneumophila* (green). At 6h p.i cells were fixed and stained for Tom20 (red), DNM1L (yellow) and nuclei (DAPI, cyan) and analysed by HCA: green, DNM1L puncta on mitochondria; red, DNM1L puncta on the cytoplasm (see Figure S4). Scale bars: 10 μm. **(B)** HCA analysis of the number of DNM1L puncta per area of mitochondria (puncta/μm^2) at 6h p.i. with WT or Δ*icmT*. Dots are replicates (each including more than 100 cells for image analysis) of a representative experiment (n=3). **(C)** hMDMs infected with WT or Δ*icmT* during indicated times, lysed and total and phosphorylated DNM1L levels analysed by Western blot. +: A549 cells treated with 20μM Forskolin for 2h (positive control). (**D**) hMDMs pre-treated or not with Mdivi1 (50 μM) during 4h, washed, stained with Mitotracker and Hoechst and infected with WT during 6h. % of infected cells is shown, dots are replicates (each including more than 100 cells for image analysis) of a representative experiment (n=3). **(E)** Same as D, % of infected cells with fragmented mitochondria. **(F)** RAW264.7 macrophages treated with siRNA against DNM1L, Ran or RanBP2 for 48h and infected with WT during 8h and analysed by HCA for mitochondrial morphology. Depletion efficiency was assessed by Western blot (Figure S4). % of infected cells with fragmented mitochondria (n=2). **(G)** Single-cell results from **F**. Each dot represents a cell (n > 50 cells per condition). (**H**) hMDMs pre-treated or not with Mdivi1 (50 μM) during 4h, washed and infected with WT. At 24h p.i., cells were lysed with sterile H_2O and GFP-expressing bacteria were quantified by flow cytometry. Relative intracellular replication, expressed as % of the control. Dots are values obtained from independent experiments (n=3). **(I)** Human A549 cells treated with siRNA oligonucleotides against DNM1L, ARF1 or RanBP2 for 48 h and infected with WT. At 24h p.i., fluorescence was measured in a plate reader. The depletion efficiency was assessed by Western blot (Figure S4). Dots are the values obtained from independent experiments (n=3). **(J)** hMDMs infected with WT or Δ*icmT* in 3 independent infections. At 6h p.i., cells were lysed and subjected to

immunoprecipitation with specific antibodies against human DNM1L. Inmunnoprecipitated lysates were analysed by label-free LC-MS/MS quantitative analysis to identify the DNM1L-interacting proteome during infection. Volcano plot of the proteins identified (black dots). Those interacting significantly with DNM1L in the three independent experiments are outside the curved volcano lines (p-value ≤ 0.05). ∗p-value ≤ 0.05; ∗∗p-value ≤ 0.01; ∗∗∗p-value ≤ 0.001; ns = non-significant (Mann-Whitney t-test).

Figure 4. *L. pneumophila*-infected human macrophages exhibit a lack of cell death signs despite *L. pneumophila*-induced mitochondrial fragmentation. (**A**) HCA analysis of apoptotic nuclei at 6h p.i. with WT or Δ*icmT*. Control: Staurosporine (STS). Counts of cells per well (sum of 16 fields) and % of cells with apoptotic nuclei are shown (n=3). (**B**) hMDMs infected with GFP-expressing *L. pneumophila* (green) during 6h, fixed and stained for Cytochrome C (CytC, red) and nuclei (DAPI, cyan). Scale bars: 10μm. (**C**) Same as in **B** but at 12h p.i. **(D)** Quantification of CytC in mitochondria of hMDM images such as in **B** and **C**. Mean Fluorescence Intensity (MFI) of CytC in mitochondria. More than 100 cells per condition were analyzed in each of the (n=3) independent experiments. **(E)** hMDMs were infected or stimulated as indicated, at 6h or 12h protein content was fractionated. CytC levels, and the quality of the fractionation (GAPDH: cytosolic control, Bcl2: mitochondrial control) were assessed by Western blot (n=2). (**F**) hMDMs infected with WT or Δ*icmT* during 6h, stained with Annexin-V-488 and analysed by flow cytometry. Dot plot Forward Scatter (FSC) vs. Side Scatter (SSC) include hMDMs in the analysis gate. Annexin-V-488 histograms of non-infected cells (red line) vs. infected cells (blue line). Control: 5% DMSO treatment (blue line, upper right histogram). (**G**) hMDMs infected with WT or Δ*icmT*, at 6h p.i. cells were incubated with FAM-YVAD-FMK during 1h to reveal active Caspase-1 imaged by confocal microscopy and analysed by HCA. Control: STS. The graph shows % of cells exhibiting active Caspase-1 (n=3). (**H**) Same as in E but at 6h p.i. cells were incubated with SR-VAD-FMK to reveal active Caspases (n=3).

Figure 5. *L. pneumophila* impairs mitochondrial respiration during infection in a T4SS- and DNM1L-dependent manner but activates glycolysis in a T4SS-independent manner. (**A**) Oxygen consumption rate (OCR) of hMDMs monitored on a Seahorse XFe96 Analyser. Basal respiration was recorded during 35 min and infection was performed by releasing WT or Δ*icmT* into each well through their corresponding ports. Mdivi1 pretreatment during 4h

was followed by washing prior to infection. % of OCR with respect to basal respiration is shown. (**B**) Bioenergetic profiles of mitochondrial respiration of WT or Δ*icmT*-infected hMDMs at 2h p.i. Oligomycin (O), FCCP (F) and Rotenone + Antimycin A (R+AA) were added sequentially into each well through their corresponding ports while OCR was monitored. See Figure S6 for interpretation of the graphs. ●: non-infected; ×: WT; ▲: Δ*icmT*. (**C**) Same as **B** but at 6h p.i. (**D**) Intracellular ATP during infection with WT, Δ*icmT*, Δ*icmT*::vector or complemented Δ*icmT*::*icmT* strains. (**E**) OCR values of hMDMs infected with different *L. pneumophila* strains and T4SS-deficient mutants (6h p.i.) (**F**) Extracellular acidification rate (ECAR) of hMDMs during infection with WT or Δ*icmT* at 1h, 2h and 5h p.i. (**G**) hMDMs pretreated or not with 2-DG or Oligomycin during 4h, washed and infected with WT. At 24h p.i., cells were lysed with sterile H_2O and GFP-expressing bacteria were quantified by flow cytometry. Relative intracellular replication is shown, expressed as % of the non-treated control (n=3). ∗p-value ≤ 0.05; ∗∗p-value ≤ 0.01; ∗∗∗p-value ≤ 0.001 (Mann-Whitney t-test).

Figure 6. *L. pneumophila* modulates mitochondrial dynamics for its efficient replication

L. pneumophila exerts highly dynamic interactions with host mitochondria and translocates the effector MitF *via* its T4SS into the cytoplasm of the macrophage. MitF is an activator of Ran GTPase, which triggers the activation of WASP and Arp2/3 with the involvement of RanBP2. Actin nucleation by WASP/Arp2/3 progressively facilitates T4SS-induced DNM1L-mediated fragmentation of host mitochondria. Whereas infection upregulates mitochondrial oxidative phosphorylation (OXPHOS) and glycolysis at 1 h post infection (p.i.) independently of the T4SS (a metabolic state represented by yellow background), *L. pneumophila*-induced T4SS-dependent mitochondrial fragmentation reduces OXPHOS while glycolysis remains active (a reprogrammed metabolic state represented by salmon background). Thus, by modulating mitochondrial dynamics, *L. pneumophila* induces a Warburg-like effect in the infected cell as early as 6 h p.i., thereby favouring its intracellular replication.

STAR★METHODS

CONTACT FOR REAGENT AND RESOURCE SHARING

Further information and requests for resources and reagents should be directed to and will be fulfilled by the Lead Contact, Carmen Buchrieser (cbuch@pasteur.fr).

EXPERIMENTAL MODEL AND SUBJECT DETAILS

Human Primary Cell Cultures

Human blood was collected by the French National Blood Service (EFS) from healthy volunteers after obtaining their informed consent and under the ethical rules established by the Ethics and Professional Conduct Committee of the EFS, which imply anonymity about the volunteers' gender, sex or age. Peripheral blood mononuclear cells (PBMCs) were isolated by Ficoll-Hypaque density-gradient separation (Lympholyte-H; Cedarlane Laboratories) at room temperature (RT). PBMCs were incubated with anti human CD14 antibodies coupled to magnetic beads (Miltenyi Biotec) and subjected to magnetic separation using LS columns (Miltenyi Biotec). Positive selected $CD14^+$ cells were counted and CD14 expression was analysed by flow cytometry, showing a rutinary purity > 90%. CD14 cells were plated in RPMI 1640 medium (Life Technologies) supplemented with 10% heat-inactivated fetal bovine serum (FBS, Biowest) in 6 well multi-dish Nunc UpCell Surface cell culture plates (Thermo Fisher) and differentiated to human monocyte-derived macrophages (hMDMs) by incubation with 50 ng/ml of recombinant human macrophage colony-stimulating factor (rhMCSF, R&D Systems) for 6 days at 37°C with 5% CO_2 in a humidified atmosphere. At day 4, additional rhMCSF (25 ng/ml) was added. After 6 days differentiation, UpCell plates were placed at 20°C during 10 minutes and hMDMs were gently detached, counted and plated in RPMI 1640 10% FBS + rhMCSF (25 ng/ml), accordingly to the specific assay performed.

Cell lines

Murine macrophage-like RAW 264.7 cells (male) and human A549 lung epithelial carcinoma cells (male) were cultivated in RPMI 1640 medium (Life Technologies) supplemented with 10% heat-inactivated FBS (Life Technologies) and 1% glutamine (Life Technologies). The cells were incubated at 37°C with 5% CO_2 in a humidified atmosphere.

Bacterial strains

L. pneumophila strain Paris or JR32 and its derivatives were grown for 3 days on N-(2-acetamido)-2-amino-ethanesulfonic acid (ACES)-buffered charcoal-yeast (BCYE) extract agar, at 37°C. For knock out and complementation constructions chloramphenicol (Cam; 5 μg/mL) was added.

METHOD DETAILS

Mitochondrial labelling

The lyophilized MitoTracker Red FM (Life Technologies) was dissolved in DMSO at 1 mM and stored it in -20°C until use it. hMDMs were plated in 384-well plates (Greiner Bio-One) at a density of 1.5 x 10^4 cells per well in 50 µl of RPMI 1640 medium (Life Technologies) supplemented with heat-inactivated 10% FBS and 20 ng/mL of rhM-CSF (Milteny) one day before the assay. Then 1 mM of MitoTracker Red FM was diluted in pre-warmed RPMI1640 without phenol-red (Life Technologies) supplemented with 100 nM glutamine (Life Technologies) and 10% FBS (assay medium). hMDMs were stained prior to infection with 40 µL of 100 nM of MitoTracker Red FM solution. After 30 minutes of incubation at 37°C/5% CO_2, cells were washed 3 times with assay medium. Between each washing step, cells were incubated at 37°C with 5% CO_2 for 5 minutes. Prior to infection the cells were washed once with pre-warmed RPMI 1640 without phenol-red.

Infection of hMDMs and automatic confocal imaging

hMDMs were infected with *L. pneumophila* grown for three days on BCYE agar plates. Bacteria were dissolved in 1X PBS (Life Technologies), the optical density (OD) was adjusted to OD_{600} of 2.5 ($2{,}2 \times 10^9$ bacteria/mL) and the bacteria were then further diluted in FBS-free RPMI 1640 medium (Life Technologies) prior to infection to obtain the respective multiplicity of infection (MOI). hMDMs were washed twice with FBS-free RPMI 1640 and then infected (MOI = 10) under transient FBS-free conditions in 384-well plates (Greiner Bio-One). The infection was synchronized by centrifugation (200 g for 5 min) and the infected cells were incubated at 37°C for 5 min in a water bath and then for 25 min at 37°C/5%CO_2. After three intensive washes with complete medium (RPMI 1640, 10% FBS) the infection proceeded in complete medium with 300 ng/mL of Hoechst H33342 (nuclear staining; Life technologies) for the respective times. Image acquisitions of multiple fields per well were performed on an automated confocal microscopes (OPERA QEHS, Perkin Elmer, or InCellAnalyzer6000, GE Health Care) using 40X or 60X objectives, excitation lasers at 405, 488, 561 and 640 nm, and emission filters at 450, 540, 600 and 690 nm, respectively. Finally, confocal images were transferred to the Columbus Image Data Storage and Analysis System (Perkin Elmer) for HCA analyses.

Inhibitors of DNM1L (Mdivi1; Tocris Bioscience), glycolysis (2-DG; Seahorse Bioscience) or oxidative phosphorylation (Oligomycin; Enzo) were added to hMDMs at the indicated concentration during 4 h prior to infection. Then, cells were washed 3 times with RPMI 1640 10% FBS and hMDMs were infected as described above.

Infection of RAW macrophages and confocal imaging

Fluorescence microscopy of RAW 264.7 macrophages was performed as described previously (Weber et al., 2006). Briefly, exponentially growing macrophages were seeded on sterile coverslips coated with poly-L-lysine (Sigma-Aldrich) in 24-well plates at 2.5×10^5 in supplemented RPMI 1640 medium and let grow over night (37°C/5%CO_2). Meanwhile, liquid cultures of *L. pneumophila* in ACES yeast extract (AYE) medium were inoculated at an OD_{600} of 0.1 and grown at 37°C for 21 h to an early stationary phase (2×10^9 bacteria/mL). Cam 5 μg/mL was added as required. RAW 264.7 macrophages were infected with dsRedExpress-producing (pCR77) *L. pneumophila* (MOI = 10) and the infection was synchronized by centrifugation (450 g, 10 min), and the infected cells were incubated at 37°C (5% CO_2) for a total of up to 8 h. The cells were then washed 1 time with 37°C RMPI and mitochondria were stained prior to fixation with 50 nM MitoTracker Deep Red FM (Life Technologies), following the manufacturer's protocol. Subsequently, the cells were fixed with 4% paraformaldehyde (PFA; Electron Microscopy Sciences) for 15 min at RT. Finally, the coverslips were washed 3 times with DPBS and mounted on glass-slides using ProLong Diamond Antifade Mountant with DAPI (Life Technologies) to stain DNA. The samples were analysed with a Leica TCS SP5 confocal microscope (HCX PL APO CS, objective 63×/1.4–0.60 oil; Leica Microsystems). Finally, confocal images were transferred to Columbus Image Data Storage and Analysis System (Perkin Elmer) for HCA analyses of mitochondrial morphology using the "project" mode of the system.

Fixed hMDMs and automatic confocal imaging

hMDMs were infected in 384-well plates as described above for living hMDMs. In the Cytochrome C experiments, 30 min before the specified time post infection, mitochondria were stained with 50 nM MitoTracker Deep Red FM (Life Technologies), following the manufacturer's protocol. Then, cells were fixed with 4% PFA for 15 min, washed with DPBS, permeabilized with DPBS-0.1% Triton-X100 for 15 min and blocked with DPBS-0.5% FBS during 30 min. Fixed cells were incubated overnight at 4°C with 30 μL of the following primary antibodies depending on the experiment: Tom20 (1:50, clone 29, BD), DNM1L (1:50; D6C7, Cell Signalling Technology) or Cytochrome C (1:50; clone 6H2.B4, BD). Cells were then washed three times with DPBS and incubated during 2 h with 50 μL of corresponding secondary antibodies: anti-mouse AlexaFluor-555 (1:500; Life Technologies),

anti-rabbit AlexaFluor-561 (1:500; Life Technologies) or anti-mouse AlexaFluor-647 (1:500; Life Technologies), and stained with DAPI (Life Technologies). Image acquisition was done as described above for hMDMs.

Acquisition of 3D time-lapse confocal movies

hMDMs were labelled for mitochondria and infected as described above using 2,5 x 10^5 hMDMs plated in 35 mm μ-Dishes (growth area = 3.5 cm2; Ibidi). hMDMs were intensively washed for 5 min after infection with RPMI 1640 10% FBS. In the case of measurements upon micro-beads phagocytosis, polystyrene-based latex 1μm Fluoresbrite 486nm microspheres (17154, Polysciences Inc.) were added (10 beads per hMDM) following the same protocol than for infecting cells. 3D time-lapse confocal movies were acquired in a Spinning-disk UltraView VOX (Perkin Elmer) using 488 and 561 lasers with 1% and 5% of laser intensity, respectively, and a maximum of 100 ms of exposure time. The whole volume of the cell was recorded by acquiring z-stack images (z = 0.3 μm) of MitoTracker-labelled hMDMs every minute using Volocity 3D imaging software (Perkin Elmer).

Western blot analyses of DNM1L and Cytochrome C

hMDMs were plated in 6 well plates (DNM1L) or 10 cm dishes (Cytochrome C), and infected at MOI=10 as described previously. At the indicated time points, cellular protein lysates for DNM1L analyses were obtained by lysis with 100 μl of 1X Blue Loading Buffer (62.5 mM Tris-HCl pH 6.8, 2% w/v SDS, 10% glycerol, 0.01% bromophenol blue and 41 mM dithiothreitol, DTT) followed by brief sonication, while protein lysates for Cytochrome C analyses were obtained after cellular fractionation using the Mitochondrial/Cytosol Fractionation kit MIT1000 (Millipore) following manufacturer instructions. After boiling lysates at 95°C during 3 min, 30μl of protein lysate were subjected to SDS-PAGE electrophoresis and transferred to Nitrocelulose membranes. Antibodies against β-Actin, Bcl2, or GAPDH were used as loading controls. The sources of the human specific antibodies were: DNM1L total (clone 22, BD), Phospho-DNM1L Ser616 (clone D9A1, Cell Signalling Technology), Phospho-DNM1L Ser637 (Sigma Aldrich), β-Actin (Sigma Aldrich), Bcl2 (MIT1000 kit, Millipore), GAPDH (MIT1000 kit, Millipore) and Cytochrome C (clone 7H8.2C12, BD, kindly supplied by F. Stavru). After 3 washes with PBS-T, membranes were incubated during 1h at RT with IRDye-800CW and IRDye-680RD-labeled secondary antibodies (Li-Cor) and scanned in an Odyssey CLx infrared digital imaging system (Li-Cor).

Immunoprecipitation and Label-free LC-MS/MS

hMDMs were plated in six 100 mm dishes (BD Falcon) at a density of 2 x 10^6 cells per dish and three dishes were infected (MOI = 10) with *L. pneumophila* JR32-WT strain while the other three dishes were infected with JR32-Δ*icmT* mutant strain. The six samples were treated independently and in parallel during the entire immunoprecipitation protocol and posterior quantitative analysis. At 6 h post infection, the medium was removed, cells were washed once with ice cold DPBS and hMDMs from each dish were harvested under non-denaturing conditions by adding to each dish 500 µL of ice cold 1X Cell Lysis Buffer (Cell Signaling Technology) supplemented with a PhosSTOP tablet (Roche) per 10 mL of Cell Lysis Buffer, incubating dishes on ice during 5 min and scrapping cells off the dishes. Cell lysate from each dish were transferred to an ice-cold micro-centrifuge tube, kept on ice, and sonicated three times for three pulses each. Then, cell lysates were centrifuged for 10 min at 4°C and 14,000 g and the supernatants were transferred to new tubes. Mouse anti human DNM1L (clone 8, BD) was added to each sample at 4 µg of antibody per mg of total protein and incubated with rotation overnight at 4°C. The following day, 20 µL of Dynabeads Protein G magnetic beads (Life Technologies) were added to each sample and incubated with rotation for 60 min at 4°C. Then, magnetic beads were pelleted using a magnetic separation rack and washed once with 1 mL ice cold 1X Cell Lysis Buffer (no PhosSTOP; Cell Signaling Technology) and 3 times with 1 mL ice cold digestion buffer (20 mM Tris pH 8.0, 2 mM $CaCl_2$), keeping samples on ice between washes. Washed beads were re-suspended in 150 µL digestion buffer and incubated for 4 h with 1 µg trypsin (Promega) at 37°C. Beads were removed, another 1 µg of trypsin was added and proteins were further digested overnight at 37°C. Peptides were purified on Omix C18 tips (Agilent), dried and re-dissolved in 20 µl 0.1% trifluoroacetic acid in water/acetonitrile (98:2, v/v) of which 2 µl was injected for LC-MS/MS analysis on an Ultimate 3000 RSLCnano system (Thermo Fisher Scientifc) in line connected to a Q Exactive mass spectrometer (Thermo Fisher Scientifc). Trapping was performed at 10 µL/min for 4 min in solvent A (0.1% formic acid in water/acetonitrile (98:2, v/v)) on a 100 µm internal diameter (I.D.) × 20 mm trapping column (5 µm beads, C18 Reprosil-HD, Dr. Maisch, Germany) and the sample was loaded on a reverse-phase column (made in-house, 75 µm I.D. x 150 mm, 3 µm beads C18 Reprosil-HD, Dr. Maisch). Peptides were eluted by a linear increase from 2 to 55% solvent B (0.08% formic acid in water/acetonitrile (2:8, v/v)) over 120 minutes at a constant flow rate of 300 nL/min. The mass spectrometer was operated in data-dependent mode, automatically switching between MS and MS/MS acquisition for the ten

most abundant ion peaks per MS spectrum. Full-scan MS spectra (400-2000 m/z) were acquired at a resolution of 70,000 in the orbitrap analyzer after accumulation to a target value of 3,000,000. The ten most intense ions above a threshold value of 17,000 were isolated (window of 2.0 Th) for fragmentation at a normalized collision energy of 25% after filling the trap at a target value of 50,000 for maximum 60 ms. MS/MS spectra (200-2000 m/z) were acquired at a resolution of 17,500 in the orbitrap analyzer The S-lens RF level was set at 50 and we excluded precursor ions with single, unassigned and charge states above five from fragmentation selection.

RNA interference, efficiency and cytotoxicity

For RNA interference experiments, A549 cells were grown in 96-well plates and treated for 48 h with a final concentration of 10 nM of siRNA oligonucleotides (see Key Resources Table). To this end, the siRNA stock (10 µM) was diluted 1:15 in RNAse-free water, and 3 µL of diluted siRNA was added per well. Allstars siRNA (Qiagen) was used as a negative control. Subsequently, 24.25 µl RPMI medium without FBS was mixed with 0.75 µL HiPerFect transfection reagent (Qiagen), added to the well, mixed and incubated for 5-10 min at RT. In the meantime, cells were diluted in RPMI medium with 10% FBS, 175 µl of the diluted cells (2 × 104 cells) were added on top of each siRNA-HiPerFect transfection complex and incubated for 48 h. RAW264.7 macrophages were transfected using AMAXA Cell Line Nucleofector Kit V (Lonza) according to the manufacturer´s recommendations, and treated for 24 h with a final concentration of 150 nM of siRNA oligonucleotides. Macrophages or epithelial cells were infected with GFP-producing *L. pneumophila* strains, and intracellular replication was determined by fluorescence as described above. The protein depletion efficiency was assessed by Western Blot. A549 cells were grown in 24-well plates and treated for 48 h with a final concentration of 10 nM of siRNA oligonucleotides. To this end, the siRNA stock (10 µM) was diluted 1:15 in RNAse-free water, and 9 µl of diluted siRNA was added per well. Allstars siRNA (Qiagen) was used as a negative control. Subsequently, 72.75 µl RPMI medium without FBS was mixed with 2.25 µl HiPerFect transfection reagent (Qiagen), added to the well, mixed and incubated for 5-10 min at RT. In the meantime, cells were diluted in RPMI medium with 10% FBS, 525 µl of the diluted cells (6×10^4 cells) were added on top of each siRNA-HiPerFect transfection complex and incubated for 48 h. RAW 264.7 cells were transfected using the AMAXA Cell Line Nucleofector Kit V (Lonza) according to the manufacturer´s recommendations, and treated

for 24 h with a final concentration of 150 nM of siRNA oligonucleotides. Protein depletion efficiency was assessed as follows: cells were harvested in ice-cold DPBS (14190144, Thermo Fisher Scientific), lysed with ice-cold NP-40 cell lysis buffer (Thermo Fisher Scientific) and cell extracts subjected to SDS-PAGE. After tank Western blotting, PVDF membranes (GE Healthcare Life Sciences) were blocked with PBS/3% BSA (bovine serum albumin, 8076.2, C. Roth) for 1 h at RT. Subsequently, specific primary antibodies against Arf1 (ab58578, Abcam), Dnm1l (ab56788, Abcam), RanBP2 (ab64276, Abcam) or GAPDH (2118, Cell Signalling) were diluted 1:500 - 1:1000 in blocking buffer and used to stain the indicated proteins (4°C, overnight). Finally, horse radish peroxidase (HRP)-conjugated secondary antibodies (GE Healthcare Life Sciences) were diluted 1:2000 in blocking buffer and incubated for 1 h at RT. After extensive washing, the enhanced chemiluminescence (EHL) signal was detected with an ImageQuant LAS4000 (GE Healthcare Life Sciences).

To assess cell viability after siRNA treatment, propidium iodide (PI)-uptake was measured. A549 cells or RAW 264.7 macrophages were grown and treated with siRNA oligonucleotides (see Key Resources Table) as described above (protein depletion efficiency). The cells were then harvested in ice cold DPBS and stained for 10 min with 1 µg/mL PI (Life Technologies) in DPBS and subjected to flow cytometry analysis (BD FACS Canto II). Gates were set according to forward/sideward scatter properties, and 10,000 events were collected for each sample. Cells treated for 10 min with 70% sterile-filtered ethanol (EtOH; Roth) served as positive control for cell death.

Intracellular replication assays

Infection of hMDMs (MOI = 10) was done in 96 well-plates and the quantification of the bacterial burden was performed by flow cytometry analysis. Infection with GFP-producing *Legionella* strains was performed as previously described for 384 well-plates by adjusting the working volumes to 96 well-plates. At 24 h post infection, supernatants were removed and stored at 4°C. Sterile deionized water was added to the cells and the plates were kept at 37°C for 1 hour until the cells were lysed. Complete cell lysis was achieved by repeated pipetting of the cell lysates, which were then recovered and mixed with the previously stored supernatants. Samples were run on a MACSQuant-VIB cytometer (Miltenyi Biotec) and the obtained data was analysed on FlowJo v 8.8.7 (Tree Star). Alternatively, cells were lysed at 24h p.i. with 50 µl of sterile deionized water and plated in BCYE plates. After 3 days of incubation at 37°C, colony-forming units (CFU) were counted.

Infection of A549 cells (MOI = 10) with GFP-producing *Legionella* strains was performed as described above. Briefly, bacteria were grown for 21 h in AYE medium, diluted in RPMI 1640 supplemented with 10% FBS/1% glutamine, centrifuged (450 *g*, 10 min, RT) and incubated for 1 h. The infected cells were washed 3 times with pre-warmed RPMI 1640 containing 10% FBS and incubated for 24 h or the time indicated (well plate was kept moist with water in extra wells). GFP fluorescence was measured using a microtiter plate reader (Synergy H1, BioTek) and results were analysed for statistical significance by the two-sample Student's t-test assuming unequal variance.

Monitoring of axenic growth of *L. pneumophila*

After 4h pre-treatment with Mdivi1 (Tocris Bioscience), 2-DG (Seahorse Bioscience) or Oligomycin (Enzo), hMDMs were washed 4 times, in order to use the same protocol as during the infection experiments with the inhibitors. After 4h pre-treatment and washing, hMDMs were lysed with 50µl of sterile deionized water. Then, *L. pneumophila* JR32-WT was added to the lysate in a minimal amount of growth medium (BYE, 5µl) and OD_{600} was automatically recorded during bacterial axenic growth, continuously shaking at 37°C, in a Synergy2 reader (BioTek).

Metabolic Extracellular Flux Analysis

hMDMs (50,000) were plated in XF-96-cell culture plates (Seahorse Bioscience). For OCR measurements, XF Assay Medium (Seahorse Bioscience) supplemented with 1 mM pyruvate and 10 mM glucose was used, and OCR was measured in a XF-96 Flux Analyzer (Seahorse Bioscience). For kinetic OCR measurements, 20 µL of *L. pneumophila* was injected through the port A in each well at an MOI = 10. For the mitochondrial respiratory control assay, hMDMs were infected at MOI = 10 and at 2 h or 6 h p.i., different drugs were injected (Mitostress kit, Seahorse Bioscience) while OCR was monitored. Specifically, Olygomycin was injected through the port A, then FCCP was injected through the port B, and finally Rotenone + Antimycin A were injected through the port C, to reach each of the drugs a final concentration in the well of 0.5 µM. For ECAR measurements, XF Base Medium (Seahorse Bioscience) was supplemented with 2 mM glutamine and ECAR was monitored in a XF-96 Flux Analyzer (Seahorse Bioscience) at indicated times during infection of hMDMs with *L. pneumophila*, MOI = 10.

Labelling of *L. pneumophila* with CFSE

L. pneumophila was stained with 9 μM Carboxyfluorescein succinimidyl ester (CFSE; Life Technologies) solution in DPBS during 20 min at 37°C with continuous agitation. Then, ice cold RPMI 1640 + 10% FBS was added and stained bacteria centrifuged at 3000 g during 10 min at RT. Supernatant was discarded and CFSE-labelled *L. pneumophila* was washed three times with ice cold DPBS and finally resuspended in FBS-free RPMI 1640 prior to infection of hMDMs.

Annexin-V detection

hMDMs were plated in 24 well multi-dish Nunc UpCell Surface cell culture plates (Thermo Fisher) at a density of 2 x 10^5 cells per well and infected with *L. pneumophila* as described above. At 6 h post infection, UpCell plates were placed at 20°C during 10 minutes and hMDMs were gently detached, collected in microcentrifuge tubes and stained with Annexin V-Alexa Fluor 488 (Life Technologies) following the manufacturer's protocol. Samples were run on a MACSQuant-VIB cytometer (Miltenyi Biotec) and the obtained data was analyzed on FlowJo v 8.8.7 (Tree Star). hMDMs treated during 6 h with 5% Dimethylsulfoxyde (DMSO; Euromedex) served as positive control for early apoptosis.

Caspase-1 and polycaspases FLICA assays and analyses

hMDMs were infected in 384-well plates, as described above, with GFP- or DsRed-expressing *L. pneumophila* for SR-VAD-FMK (polycaspases; Life Technologies) or FAM-YVAD-FMK (Caspase-1; Immunochemisitry Technologies) FLICA assays, respectively. At 6 h post infection, FLICA reagent was added to the cells and incubated during 1 h at 37°C/5% CO_2. Then, hMDMs were washed once with DPBS, fixed with 4% PFA during 15 min at RT and stained with DAPI (Life Technologies). Image acquisitions of multiple fields per well were performed on an automated confocal microscope (OPERA QEHS, Perkin Elmer) using 40X objective, excitation lasers at 405, 488, 561 and 640 nm, and emission filters at 450, 540, 600 and 690 nm, respectively, and images were transferred to Columbus Image Data Storage and Analysis System (Perkin Elmer).

QUANTIFICATION AND STATISTICAL ANALYSIS

Statistical analyses

The two-sample Student’s t-test (Mann-Whitney test, not assumption of Gaussian distributions) was used in all data sets unless the contrary is specified in the Methods Details section. Data analysis was performed using Prism v5 (Graphpad Software). The exact value

of “n” is specified in the figure legends and represents the number of independent experiments performed except for those panels showing single cell results (1F, 2G and 3G), where “n” represents the number of analysed cells per condition.

Automatic High-Content Analyses

All the analyses were performed on Columbus Image Data Storage and Analysis System (Perkin Elmer) using in-house developed scripts (shared upon request). For the HCA of the subcellular localization of mitochondria, the Hoechst signal was used to segment nuclei in the 405/450 channel (excitation/emission), MitoTracker low signal in the 561/600 channel was used to segment the cytoplasm region and, after filtering the 561/600 channel using the sliding parabola method for background removal, the high intensity Mitotracker signal was used to segment mitochondria. *L. pneumophila* was identified by measuring the GFP signal in the 488/540 channel and a virtual vacuole was established at 1 μm distance around each bacterium identified. Finally, the single cell analysis of LCV-mitochondria contacts was performed by quantifying the number of identified mitochondria inside this virtual vacuole (see also Figure 1).

For the HCA of the mitochondrial morphology, the Hoechst signal was used to segment nuclei in the 405/450 channel, while the MitoTracker signal in the 561/600 channel was used to segment the cytoplasmic region. *L. pneumophila* was identified by measuring the GFP signal in the 488/540 channel. Two populations - the infected cells and the non-infected bystander cells - were defined by max GFP fluorescent intensity of each cell. The single cell analysis of the mitochondrial morphology was performed by applying the SER texture algorithm to define the cytoplasm region (mainly SER Edge and SER Ridge, normalization by regional intensity) in the 561/600 channel (filtered by sliding parabola method, background removal). For the *classical* mitochondrial morphological analyses, mitochondria were segmented using the 561/600 channel (filtered by the sliding parabola method, background removal) and morphological properties of segmented mitochondria were measured. For the HCA of the mitochondrial morphology in RAW 264.7 macrophages, the identification of *L. pneumophila* was performed using the DsRed signal in the 561/600 channel and the single cell analysis of the mitochondrial morphology was performed by applying SER texture algorithms to define the cytoplasm region (SER Edge and SER Ridge, normalization by regional intensity) in the 640/690 channel filtered by sliding parabola method for background removal (see also Figure 2 and S3).

For the HCA of DNM1L recruitment to mitochondria, the DAPI signal was used to segment nuclei in the 405/450 channel, while the Tom20 low signal in the 640/690 channel was used to segment the cytoplasm and high intensity Tom20 signal was used to segment mitochondria. *L. pneumophila* was identified by measuring the GFP signal in the 488/540 channel and thereby infected and non-infected cells were defined. The single cell analysis of DNM1L puncta on mitochondria was performed by identifying DNM1L puncta using the 561/600 channel. Selection of DNM1L puncta on mitochondria was performed using the 640/690 channel (Tom20). Subcellular structures positive for both signals (DNM1L and Tom20) were considered DNM1L puncta on mitochondria, and the number of DNM1L puncta was measured in each infected cell (see also Figure S4).

For the HCA of apoptotic nuclei, the Hoechst signal was used to segment nuclei in the 405/450 channel and the identification of *L. pneumophila* was performed using the GFP signal in the 488/540 channel. Then the nuclei size and the Hoechst signal intensity was measured in each infected or non-infected cell, and small and bright nuclei were considered as apoptotic ones.

For the HCA analyses of Caspase-1 or polycaspase activation, the DAPI signal was used to segment nuclei in the 405/450 channel. For the Caspase-1 activity assay, the identification of *L. pneumophila* was performed using the DsRed signal in the 561/600 channel, and the FAM-YVAD-FMK mean fluorescence intensity in the 488/540 channel was measured in each infected cell. For the polycaspases activity assay, the identification of *L. pneumophila* was performed using GFP signal in the 488/540 channel, and SR-VAD-FMK mean fluorescence intensity in the 561/600 channel was measured in each infected cell. hMDMs treated during 6 h with 2µM Staurosporine (Sigma-Aldrich) served as positive control for caspases activation.

Analyses of 3D time-lapse confocal movies

To quantify statistically the contacts between the LCV and mitochondria in 3D time lapse confocal microscopy we developed a new point-process approach that is based on the statistical analysis of the Ripley's K function. The first step of this method is the automatic detection of LCV and mitochondria with a wavelet-based method that extracts the fluorescence signal that is significantly brighter than background (Olivo-Marin, 2002). This method is implemented in the plugin *Spot Detector* in the open-source image analysis software Icy, available at http://icy.bioimageanalysis.org/ (de Chaumont et al., 2012).

The second step of this method was the statistical characterization of the distances between detected spots. To test whether certain mitochondria are significantly closer to the LCV at time *t*, meaning. that mitochondria are not just randomly distributed in the cell cytoplasm and close to the LCV by chance, we computed the Ripley's K function at each time *t* between the positions (centres of mass) of LCV ($n_1(t)$ LCV inside the cell at time *t*, positions *x(t)*) and mitochondria ($n_2(t)$ detected mitochondria, positions *y(t)*) :

$$K(x,y,t)(r) = \frac{\text{Cell Volume}}{n_1 n_2}(t) \sum_{x,y} \mathbf{1}\left\{d(x(t),y(t)) < r\right\} b(x(t),y(t),r)$$

For a distance parameter *r*, the K function counts the number of positions *y(t)* that are at a distance < *r* from *x(t)* positions. The term *b(x,y,r)* is a boundary correction term that accounts for the expected fewer neighbours of LCV that are close to the cell boundary. To test whether K function is significantly high, we characterized its statistical distribution under the null hypothesis of a random distribution of mitochondria. We have previously shown that K function is normally distributed (Lagache et al., 2015) and that the expected mean μ(r) of K function, when spots are randomly distributed, is the volume of the ball of radius r ($4/3.\pi.r^3$). We computed here the variance v(r) of the K function and built a statistical test with

$$\max_{0 \leq r \leq r_{max}} \frac{K(x,y,r) - \mu(r)}{\sqrt{v(r)}}$$

Then, we measured the percentage of mitochondria that are statistically close (coupled) to LCV by performing a parametrical fitting of the K function. Our statistical method is implemented and freely available in the plugin *Colocalization Studio* in Icy. The analysis of the Mitotracker that we saw transferring from mitochondria to LCVs (Figure S2) was performed using Volocity 3D imaging software (Perkin Elmer) by identifying *L. pneumophila*-GFP in the 488 channel, segmenting 3D bacteria inside the infected cell and measuring MitoTracker signal in the 561 channel inside 3D bacteria in each time point of the time lapse.

Label-free LC-MS/MS quantitative analysis

For protein identification and quantification, data analysis was performed with MaxQuant (version 1.5.4.1) (Cox and Mann, 2008) using the Andromeda search engine with default search settings including a false discovery rate set at 1% on both the peptide and protein level. Spectra were searched against two reference proteome databases downloaded from Uniprot (http://www.uniprot.org/). The first database contained 2,930 proteins from *Legionella*

pneumophila strain Philadelphia 1 (taxID 272624, proteome ID UP000000609) and the second database contained 20,198 proteins from *Homo sapiens* (taxID 9606, proteome ID UP000005640). The mass tolerance for precursor and fragment ions was set to 4.5 and 20 ppm, respectively, during the main search. Enzyme specificity was set as C-terminal to arginine and lysine, also allowing cleavage at proline bonds with a maximum of three missed cleavages. Variable modifications were set to oxidation of methionine residues, acetylation of protein N-termini, phosphorylation of serine, threonine and tyrosine residues and diglycine modification of lysine residues. Only proteins with at least one unique or razor peptide were retained leading to the identification of 559 proteins. Proteins were quantified by the MaxLFQ algorithm integrated in the MaxQuant software (Cox et al., 2014). A minimum ratio count of two unique or razor peptides was required for quantification. Further data analysis was performed with the Perseus software (version 1.5.2.4) after loading the protein groups file from MaxQuant. Proteins only identified by site, reverse database hits and contaminants were removed and replicate samples of both conditions were grouped. Proteins with less than three valid values in at least one group were removed and missing values were imputed from a normal distribution around the detection limit. Then, a t-test was performed for pairwise comparison of both conditions. The results of this t-test is shown by the volcano plot in Figure 3H. For each protein, the $\log_2$ (Δ*icmT*/WT) fold change value is indicated on the X-axis, while the statistical significance (-log p-value) is indicated on the Y-axis. Proteins outside the curved lines, set by an FDR value of 0.05 and an S0 value of 1 in the Perseus software, represent specific DNML1 interaction partners in macrophages, binding only after infection with either the JR32-WT or the JR32-Δ*icmT* strain.

Analyses of Flow Cytometry data

Obtained cytometry data was analysed on FlowJo v 8.8.7 (Tree Star).

CellPress

TABLE FOR AUTHOR TO COMPLETE

Please upload the completed table as a separate document. ***Please do not add subheadings to the Key Resources Table.*** *If you wish to make an entry that does not fall into one of the subheadings below, please contact your handling editor. (**NOTE:** For authors publishing in Current Biology, please note that references within the KRT should be in numbered style, rather than Harvard.)*

KEY RESOURCES TABLE

REAGENT or RESOURCE	SOURCE	IDENTIFIER
Antibodies		
MicroBeads conjugated to monoclonal anti-human CD14	Miltenyi Biotec	Cat#130-050-201
Mouse monoclonal anti-Tom20	BD	Clone 29
Rabbit monoclonal DNM1L (IF)	Cell Signalling	Clone D6C7
Mouse monoclonal anti-Cytochrome C (IF)	BD	Clone 6H2.B4
Mouse monoclonal anti-DNM1L (WB)	BD	Clone 22
Mouse monoclonal anti-Phospho-DNM1L Ser616	Cell Signalling	Clone D9A1
Rabbit polyclonal Phospho-DNM1L Ser637	Sigma Aldrich	Cat# SAB4301399
Rabbit polyclonal β-Actin	Sigma Aldrich	Cat# A2066
Mouse monoclonal anti-Bcl2	Millipore	MIT1000 kit
Mouse monoclonal anti-GAPDH	Millipore	MIT1000 kit
Mouse monoclonal anti-Cytochrome C (WB)	BD, kindly supplied by F. Stavru (I. Pasteur)	Clone 7H8.2C12
Goat polyclonal anti-ARF1	Abcam	Cat# ab58578
Mouse monoclonal anti-DNM1L (WB, Figure S7)	Abcam	Cat# ab56788
Rabbit polyclonal anti-RanBP2	Abcam	Cat# ab64276
Rabbit monoclonal anti-GAPDH	Cell Signalling	Clone 14C10
Bacterial and Virus Strains		
JR32-WT, Virulent *L. pneumophila* serogroup 1 strain Philadelphia	Sadosky A.B., *et al.,* 1993	N/A
JR32- Δ*icmT*, *L. pneumophila* JR32 *icmT3011*::Kan^R	Segal G. and Shuman H.A.,1998	N/A
JR32-Δ*mitF*, JR32 *legG1*::Kan^R	Rothmeier E., *et al.,* 2013	N/A
JR32- Δ*mitF::mitF,* JR32 *legG1*-M45-LegG1::Kan^R	Rothmeier E., *et al.,* 2013	N/A
Lpp-WT, Virulent *L. pneumophila* serogroup 1 strain Paris	Cazalet C., *et al.,* 2004	N/A
Lpp- Δ*dotA*, *L. pneumophila* Paris *dotA*::Kan^R	This paper	N/A
Chemicals, Peptides, and Recombinant Proteins		
Recombinant human macrophage colony-stimulating factor (rhMCSF)	R&D Systems	Cat# 216-MC-025
Mdivi1	Tocris Bioscience	Cat# 3982
2-DG	Seahorse Bioscience	Cat# 103020-100
Oligomycin	Enzo	Cat# ALX-380-037
Carboxyfluorescein succinimidyl ester (CFSE)	Life Technologies	Cat# C34554
Critical Commercial Assays		
Mitochondrial/Cytosol Fractionation kit	Millipore	MIT1000
Caspase-1 FLICA assay	Immunochemisitry Technologies	Cat# 98
Polycaspases FLICA assay	Life Technologies	Cat# I35101

Experimental Models: Cell Lines		
Murine macrophage-like RAW 264.7 cells	ATCC	RRID: CVCL_0493
Human A549 lung epithelial carcinoma cells	ATCC	RRID: CVCL_0023
Biological samples		
Human blood from healthy donors	EFS	N/A
Recombinant DNA		
pCR77, pMMB207C-P_{tac}-RBS-*dsred*-RBS-MCS	Finsel I., *et al.* 2013	N/A
pNT28, pMMB207-C, Δ lacIq (constitutive gfp, -GFP)	Tiaden A., *et al*. 2007	N/A
pER5, pCR77-M45-*legG1*	Rothmeier E., *et al.*, 2013	N/A
Oligonucleotides		
See Table S1		
Software and Algorithms		
Columbus Image Data Storage and Analysis System	Perkin Elmer	Part # Columbus
In-house developed HCA scripts for Columbus	This paper	Shared upon request
ICY, open-source image analysis software	http://icy.bioimageanalysis.org/	v. 1.8.6.0
Other		
Nunc UpCell Surface cell culture plates (6W)	Thermo Fisher	Cat# 174901
Nunc UpCell Surface cell culture plates (24W)	Thermo Fisher	Cat# 174899

Figure 1

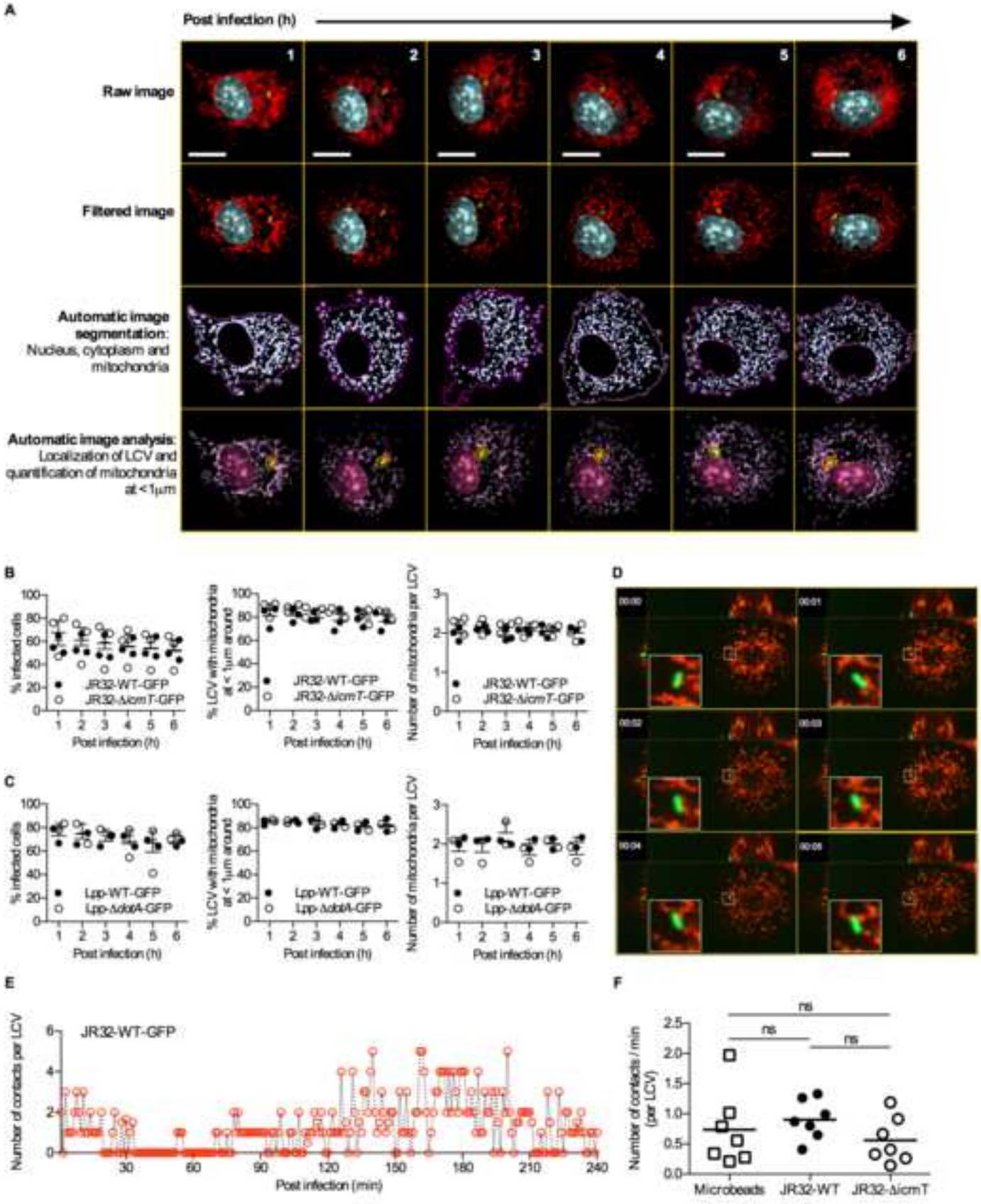

Figure 2

Click here to download Figure Figure 2-R1.tiff

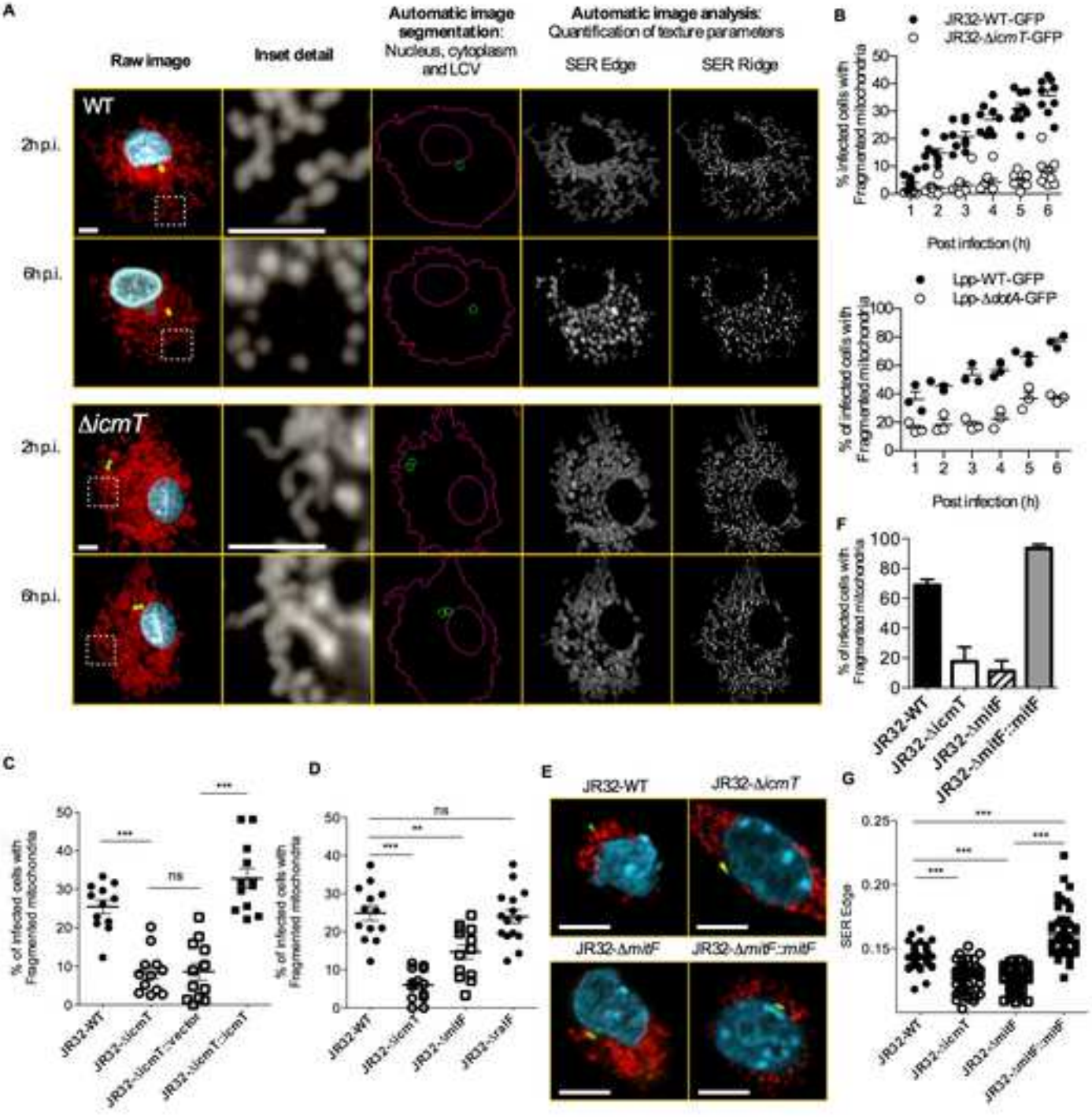

Figure 3

Click here to download Figure Figure3.tiff

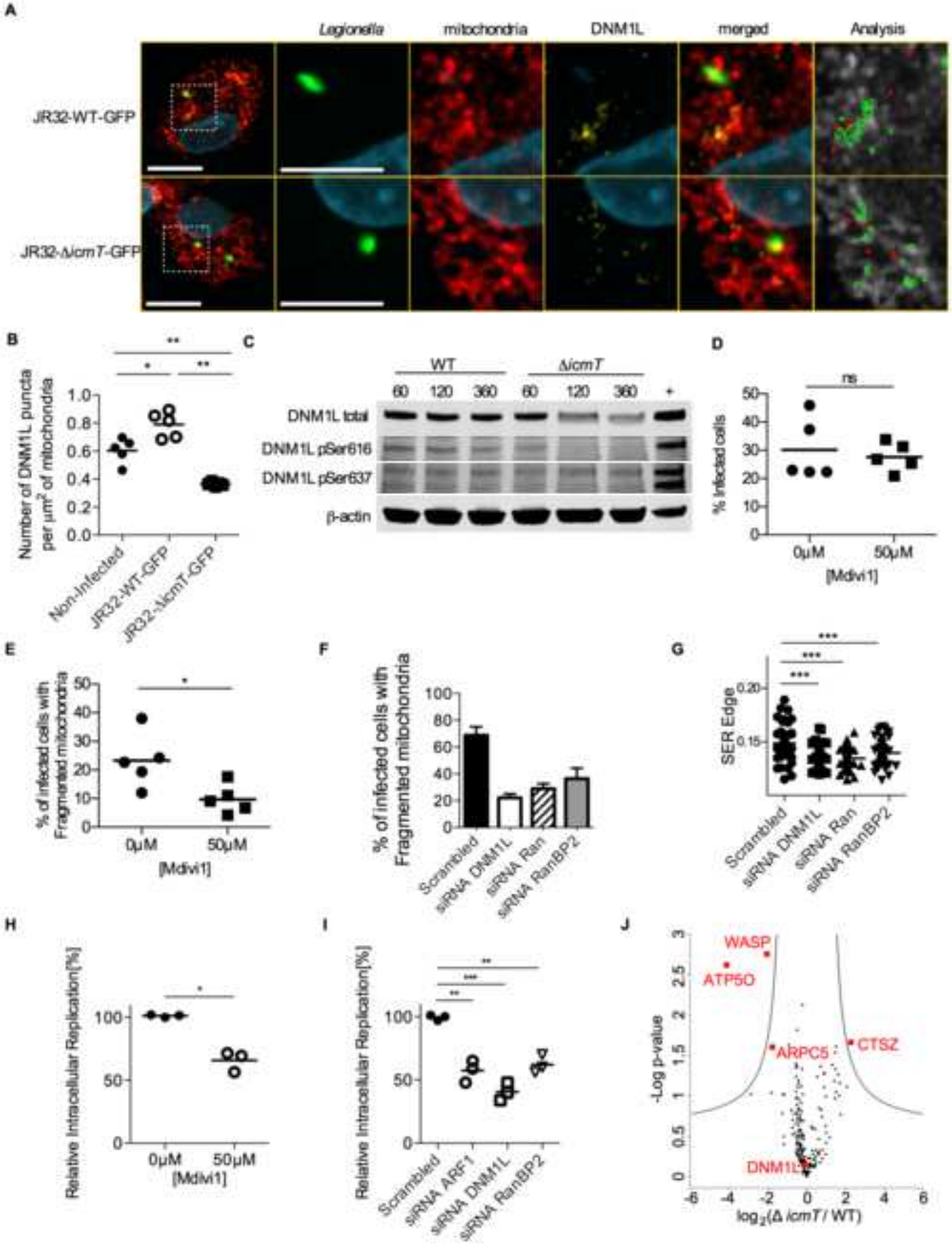

Figure 4

Click here to download Figure Figure 4_R1.tiff

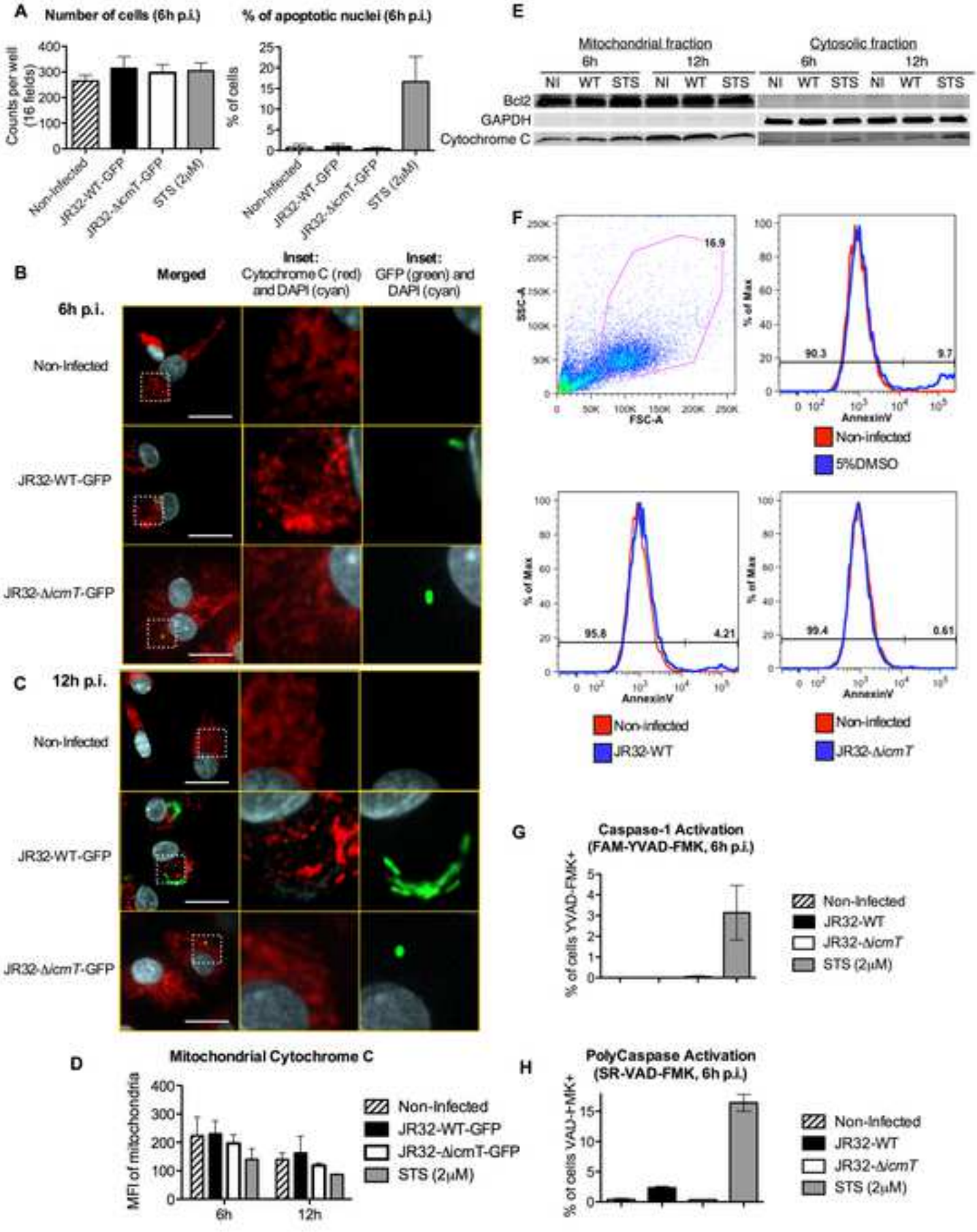

Figure 5

Click here to download Figure Figure 5_R1.tiff

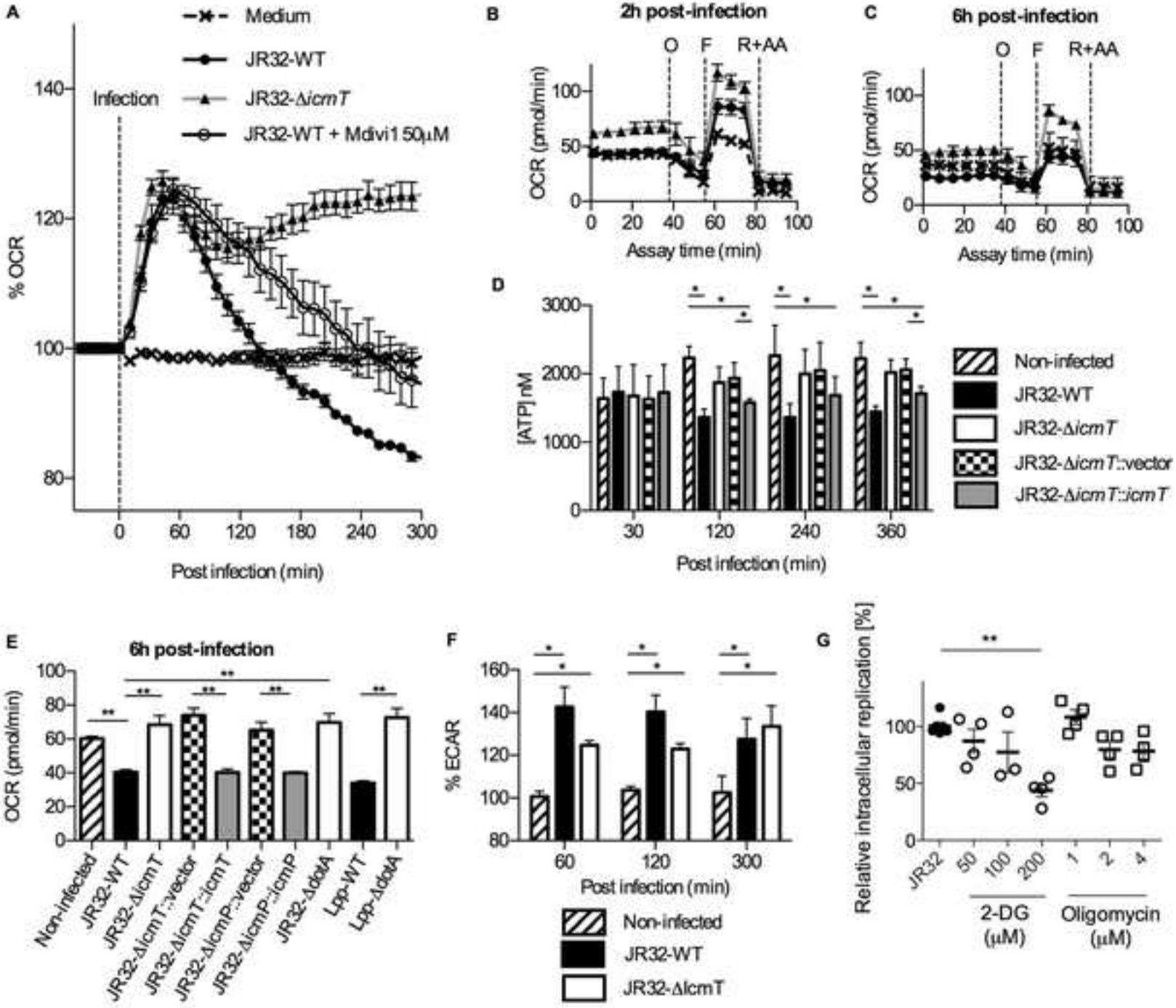

Figure 6

Click here to download Figure Figure 6_R1.tiff

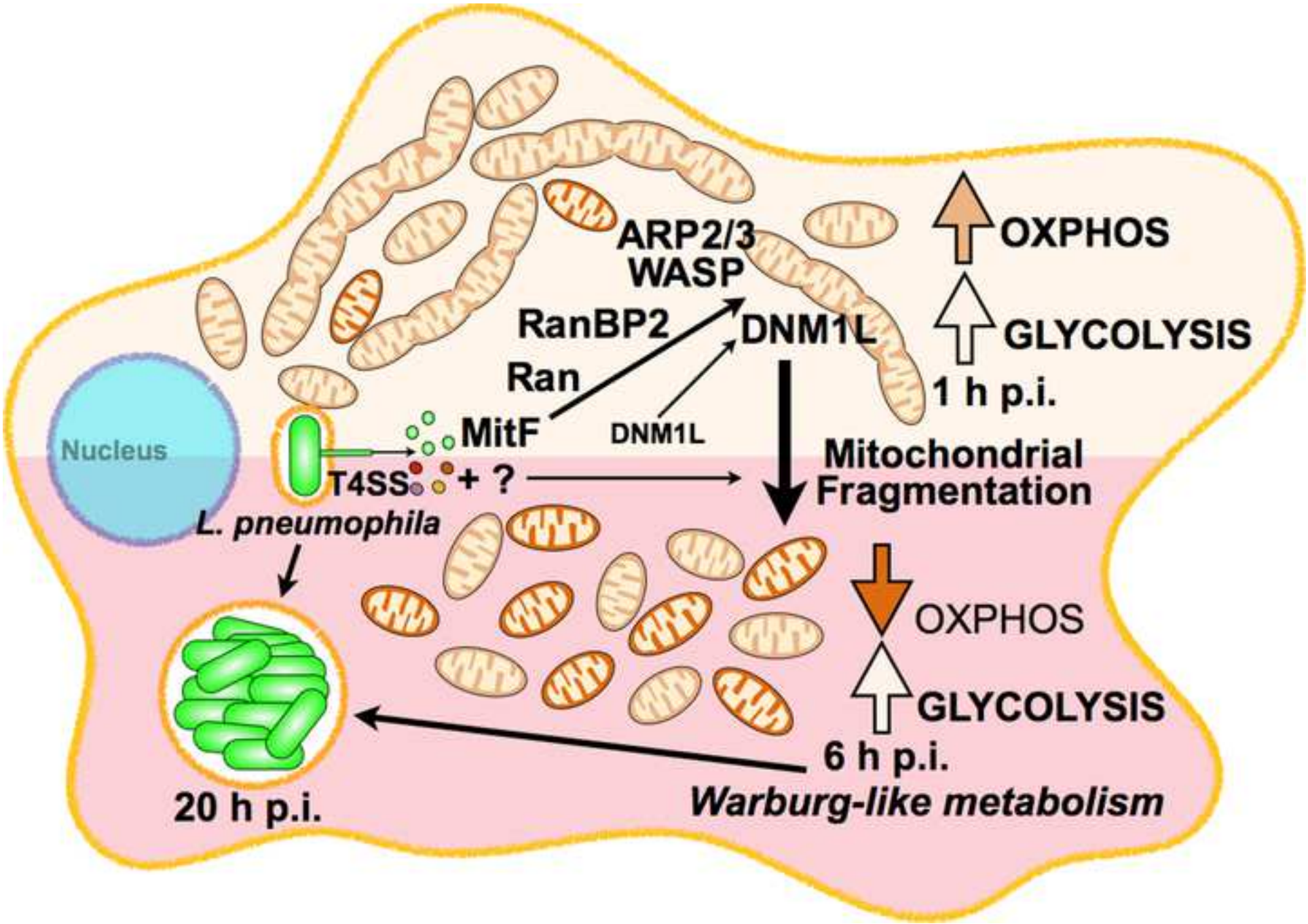

Supplementary Information

Legionella pneumophila modulates mitochondrial dynamics to trigger metabolic repurposing of infected macrophages

Pedro Escoll[1,2], Ok-Ryul Song[3], Flávia Viana[1,2], Bernhard Steiner[4], Thibault Lagache[5,6], Jean-Christophe Olivo-Marin[5], Francis Impens[7,8,9], Priscille Brodin[3], Hubert Hilbi[4] & Carmen Buchrieser[1,2]

[1]Institut Pasteur, Biologie des Bactéries Intracellulaires and [2]CNRS UMR 3525, Paris, France, [3]Univ. Lille, CNRS, Inserm, CHU Lille, Institut Pasteur de Lille, U1019 – UMR 8204-CIIL-Center for Infection and Immunity of Lille, F-59000 Lille, France, [4]Institute of Medical Microbiology, University of Zurich, Switzerland, [5]Institut Pasteur, Unité d'Analyse d'Images Biologiques, CNRS UMR 3691, Paris, France, [6]Present address: Department of Biological Sciences, Columbia University, 10027 New-York, [7]VIB-UGent Center for Medical Biotechnology, and [8]VIB Proteomics Core and [9]Department of Biochemistry, Ghent University, 9000 Ghent, Belgium[10] These authors contributed equally, [11]Lead contact

Figure S1: Related to Figure 1. Quantification of *Legionella*-mitochondria contacts in hMDM cells during infection.

Figure S2: Related to Figure 1. Transfer of Mitotracker dye from mitochondria to the LCV occurred occasionally during the dynamic contacts.

Figure S3: Related to Figure 2. Mitochondrial morphology parameters change during infection but not the total mitochondrial mass

Figure S4. Related to Figure 3**.** DNM1L is implicated in mitochondrial changes due to *L. pneumophila* infection in different cell types.

Figure S5. Related to Figure 3 and 5. Mdivi-1, 2-DG and Olygomycin pre-treatment has no effect on axenic growth of *L. pneumophila*.

Figure S6. Related to Figure 5. Bioenergetic profiles of the key parameters of mitochondrial respiration change due to *L. pneumophila* infection.

Table S1: Oligonucleotides used for RNA interference.

Movie S1: Related to Figure 1. 3D confocal time-lapse movie of a JR32-WT-GFP-infected hMDM cell.

Movie S2: Related to Figure 1. 3D confocal time-lapse movie of a JR32-Δ*icmT*-GFP-infected hMDM cell.

Movie S3: Related to Figure 1. Reconstruction of 3D confocal z-stack time-lapse movie of a JR32-WT-GFP-infected hMDM cell.

Movie S4: Related to Figure 1. 3D confocal time-lapse movie of a microbeads-"infected" hMDM cell.

Movie S5: Related to Figure 1. Transfer of Mitotracker dye from mitochondria to the LCV occurred occasionally during the dynamic contacts.

Figure Legends:

Figure S1. Related to Figure 1. **Quantification of *Legionella*-mitochondria contacts in hMDM cells during infection**. Number of contacts per LCV during a time course are shown (A) JR32-WT-GFP and (B) JR32-Δ*icmT*-GFP. The statistical method used is described in the STAR methods. See also Movies S1 and S2.

Figure S2. Related to Figure 1**. Transfer of Mitotracker dye from mitochondria to the LCV occurred occasionally during the dynamic contacts**. **(A)** 3D confocal time-lapse images of a JR32-WT-GFP-infected hMDM previously labelled with MitoTracker (Movie S3). Mitochondria (red) and *Legionella* (green) are shown. For the analysis, 3D intracellular bacteria were identified in the 488 channel, labelled as JR32-WT-1, -2 and -3 in the figure. At 4 min p.i., JR32-WT-2 contacted mitochondria (white arrow head). At 29 min p.i. JR32-WT-2 have intensively acquired MitoTracker dye (white asterisk), in contrast to the other two LCVs within the hMDM. Scale bar: 2.40 μm **(B)** Quantification of the mean fluorescence intensity (MFI) inside 3D bacteria in the 488 and 561 channels. Arrowhead indicates the contact of JR32-WT-2 with mitochondria.

Figure S3. Related to Figure 2. **Mitochondrial morphology parameters change during infection but not the total mitochondrial mass**. **(A)** HCA Analysis of hMDMs at 2 h (left) or 6h p.i (right) is shown for the same individual cells. Application of texture algorithms to mitochondrial signal converts texture into values, which normally change during changes in mitochondrial morphology. **(B)** To correlate SER values to specific mitochondrial morphologies, 10 cells are selected in each experiment with clear non-fragmented or fragmented morphologies and SER values are plotted. The cut-off of the fragmented phenotype is set just above the mean of the SER value of the fragmented phenotype. This should be done for each individual experiment, as small differences in parameters such as mean mitochondrial intensity, microscope or magnification used, as well as hMDM from different donors alter SER values between different experiments. **(C)** Plots of SER values of hMDMs infected with *L. pneumophila* JR32-WT-GFP or JR32-Δ*icmT*-GFP in the same experiment as in B. In this experiment, both SER-Edge and SER-Ridge are used to distinguish changes in mitochondrial morphology. **(D)** Classical morphology measurements using a mitochondrial segmentation strategy in the same experiment as in B. Instead of analysing texture of mitochondrial channel, the channel was used to segment individual mitochondria and different morphological measurements were performed. **(E)** Mitochondrial mass during *L. pneumophila* infection. hMDMs were infected with *L. pneumophila* JR32-WT, JR32-Δ*icmT*

mutant or left uninfected. At 6h, cells were stained with the membrane-potential independent dye Mitotracker Green (MTG), detached from the plates and analysed by Flow Cytometry. Mean Fluorescence Intensity (MFI) of MTG is shown. ∗p-value ≤ 0.05; ∗∗p-value ≤ 0.01; ∗∗∗p-value ≤ 0.001; ns = non-significant (Mann-Whitney t-test).

Figure S4. Related to Figure 3**. DNM1L is implicated in mitochondrial changes due to *L. pneumophila* infection in different cell types. (A)** High Content Analysis of DNM1L association with host mitochondria during infection of hMDMs with *L. pneumophila*. The steps of the analysis are depicted. 1: Raw image. 2: Segmentation of nuclei and cytoplasm using DAPI channel (405). 3a: GFP channel (488), localization of LCV. 3b: Mitotracker channel (633), localization of mitochondria. 3c: DNM1L channel (565), localization of DNM1L puncta. Combination of 3a and 3c renders 4: Identification of DNM1L puncta in infected cells. 5: Identification of DNM1L puncta in the cytoplasm (red puncta) and DNM1L puncta co-localizing with mitochondria (green puncta). Quantification of whole cell mitochondria area from step 3b and number of mitochondria-associated DNM1L puncta provide numbers of DNM1L puncta per μm^2 of host mitochondria. **(B)** *L. pneumophila* induces T4SS-dependent changes in mitochondrial morphology during infection of A549 cells. A549 cells were stained with Mitotracker (red), infected with GFP-expressing *L. pneumophila* WT or Δ*icmT* mutant (green) and their nuclei stained with Hoechst dye (cyan). Living cells were imaged by confocal microscopy each hour and analysed by HCA. **(C)** HCA analysis of mitochondrial morphology during JR32-WT-GFP or JR32-Δ*icmT*-GFP infection of A549 cells. Percentage of infected cells with fragmented mitochondria is shown (n = 3). **(D)** Related to Figure 3H. hMDMs were pre-treated or not with Mdivi1 (50 or 100 μM) during 4h, washed and infected with *L. pneumophila* JR32-WT or JR32-Δ*icmT*. At 24h p.i., cells were lysed with 50 μl of sterile distilled water and plated in BCYE plates. After 3 days of incubation at 37°C, colony-forming units (CFU) were counted. Results are expressed as CFU per ml of lysis volume (n=3). **(E)** Western blot analysis of target protein depletion in A549 cells. Human A549 cells were treated with 2 or 4 different siRNA oligonucleotides (Oligo 1-4) against DNM1L, RanBP2 or Arf1 for 48 h. The depletion efficiency was assessed by Western blot using specific antibodies against indicated proteins. GAPDH served as a loading control. Qiagen AllStars oligonucleotides were used as a negative control (scrambled). **(F)** Western blot analysis of target protein depletion in RAW264.7 macrophages. Murine RAW264.7 macrophages were treated with a mix of 4 different siRNA oligonucleotides against DNM1L, Ran, or RanBP2 for 24h. The depletion efficiency was

assessed by Western blot using specific antibodies against indicated proteins. GAPDH served as a loading control. Qiagen AllStars oligonucleotides were used as a negative control (scrambled). **(G)** Cytotoxicity of siRNA treatment. Human A549 epithelial cells were treated with 4 different siRNA oligonucleotides (oligo 1-4) against DNM1L or RanBP2 for 48h. Cells treated with scrambled siRNA served as negative control, silencing of Arf1 served as positive control. 70% EtOH was used as control for cell death. Qiagen AllStars oligonucleotides (scrambled) were used as baseline for the experiment. Data represent the means and SEM of two independent experiments. PI: propidium iodide.

Figure S5. Related to Figure 3 and 5. **Mdivi-1, 2-DG and Olygomycin pre-treatment has no effect on axenic growth of *L. pneumophila***. hMDMs were not pretreated (control, A) or pre-treated during 4h with Mdivi-1 (B), 2-DG (C) or Olygomycin (D). After 4h pretreatment, hMDMs were washed, in order to use the same protocol as for the results depicted in Figure 3 and 5. After 4h pretreatment and washing, hMDMs were lysed with 50µl of distilled water. Then, *L. pneumophila* WT was added to the lysate in a minimal amount of growth medium (BYE, 5µl) and the OD_{600} was automatically recorded during bacterial axenic growth (continuously shaking at 37°C). Panels A, B, C and D show OD_{600} over time of 12 replicates from 2 independent experiments. Panel E shows the comparison of the different conditions by showing the mean of all the replicates of each condition.

Figure S6. Related to Figure 5. **Bioenergetic profiles of the key parameters of mitochondrial respiration change due to *L. pneumophila* infection (A)** Bioenergetic profiles of the key parameters of mitochondrial respiration during mitochondrial respiratory control assay using the Seahorse XF Mitostress kit. Sequential compound injections measure basal respiration, ATP production, proton leak, maximal respiration, spare respiratory capacity, and non-mitochondrial respiration (Source: Seahorse Bioscience). **(B)** Contribution of *L. pneumophila* to oxygen consumption rate (OCR) measurements during infection is minimal. OCR of *L. pneumophila* WT alone (quantity for MOI=10), hMDMs alone or WT-infected hMDMs (4h p.i.) was measured on a Seahorse XFe96 Analyser. Results show 3 independent experiments, each one having 4 replicates. Note the break in the Y axe. The table shows mean and standard deviation of the 3 experiments. **(C)** Contribution of *L. pneumophila* to ATP measurements during infection is minimal. ATP of *L. pneumophila* WT alone (quantity for MOI=10) or hMDMs alone was measured. Results show 2 independent

experiments, each one having 3 replicates. Note the break in the Y axe. The table shows mean and standard deviation of the 2 experiments.

Movie legends:

Movie S1: Related to Figure 1. 3D confocal time-lapse movie of a JR32-WT-GFP-infected hMDM cell. The movie shows the highly dynamic *Legionella*-mitochondria contacts during 24 minutes. Details shown on the left.

Movie S2: Related to Figure 1. 3D confocal time-lapse movie of a JR32-Δ*icmT*-GFP-infected hMDM cells. The movie shows highly dynamic *Legionella*-mitochondria contacts during 24 minutes. Details shown on the left.

Movie S3: Related to Figure 1. Reconstruction of 3D confocal z-stack time-lapse movie of a JR32-WT-GFP-infected hMDM cells. The movie shows highly dynamic *Legionella*-mitochondria contacts during 197 minutes. The movie is repeated 3 times. Non-reconstructed time-lapse movie is shown in the inset.

Movie S4: Related to Figure 1. 3D confocal time-lapse movie of a microbeads ”infected” hMDM cell. The movie shows the highly dynamic *microbeads*-mitochondria contacts during 24 minutes.

Movie S5: Related to Figure 1. 3D confocal time-lapse movie of a JR32-WT-GFP-infected hMDM cell. The movie shows the transfer of Mitotracker dye from mitochondria to the LCV during 29 min of infection. The movie is repeated 3 times. The arrow indicates the increment of MitoTracker dye in a LCV after the contact with mitochondria

Table S1. Oligonucleotides used for RNA interference

NCBI gene	Gene description	Entrez Gene ID	Product name	Product ID
Unspecific_AllStars_1	AllStars (*Scrambled*)	0	Unspecific_AllStars_1	SI03650318
ARF1	ADP-ribosylation factor 1	375	Hs_ARF1_1 (1)	SI00299250
			Hs_ARF1_10 (2)	SI02757272
RanBP2	Ran binding protein 2	5903	Hs_RANBP2_6 (1)	SI03117310
			Hs_RANBP2_5 (2)	SI03043901
			Hs_RANBP2_4 (3)	SI00698264
			Hs_RANBP2_2 (4)	SI00698250
DNM1L	Dynamin 1-like	10059	Hs_DNM1L_10 (1)	SI04320092
			Hs_DNM1L_9 (2)	SI04274235
			Hs_DNM1L_8 (3)	SI04202464
			Hs_DNM1L_4 (4)	SI02661365
Arf1	ADP-ribosylation factor 1	11840	Mm_ARF1_4 (1)	SI00901656
RanBP2	Ran binding protein 2	19386	Mm_Ranbp2_1 (1)	SI01396703
			Mm_Ranbp2_2 (2)	SI01396710
			Mm_Ranbp2_3 (3)	SI01396717
			Mm_Ranbp2_4 (4)	SI01396724
DNM1L	Dynamin 1-like	74006	Mm_Dnm1l_1 (1)	SI00982219
			Mm_Dnm1l_2 (2)	SI00982226
			Mm_Dnm1l_3 (3)	SI00982233
			Mm_Dnm1l_4 (4)	SI00982240
Ran	RAN, member RAS oncogene Family	19384	Mm_Ran_1 (1)	SI00184366
			Mm_Ran_3 (2)	SI00184380
			Mm_Ran_4 (3)	SI00184387
			Mm_Ran_7 (4)	SI0271092

Figure S1

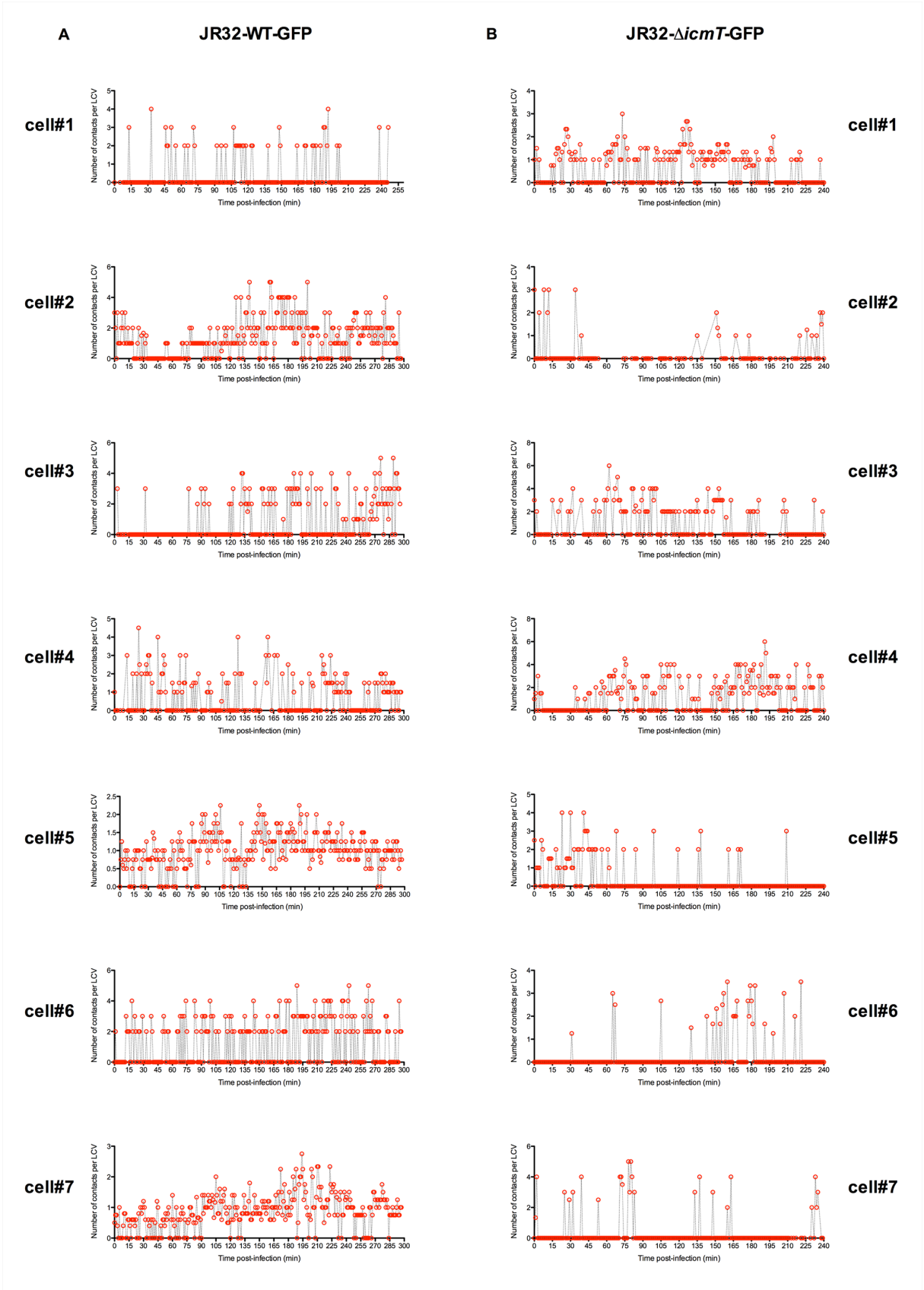

Figure S1. Related to Figure 1.

Figure S2

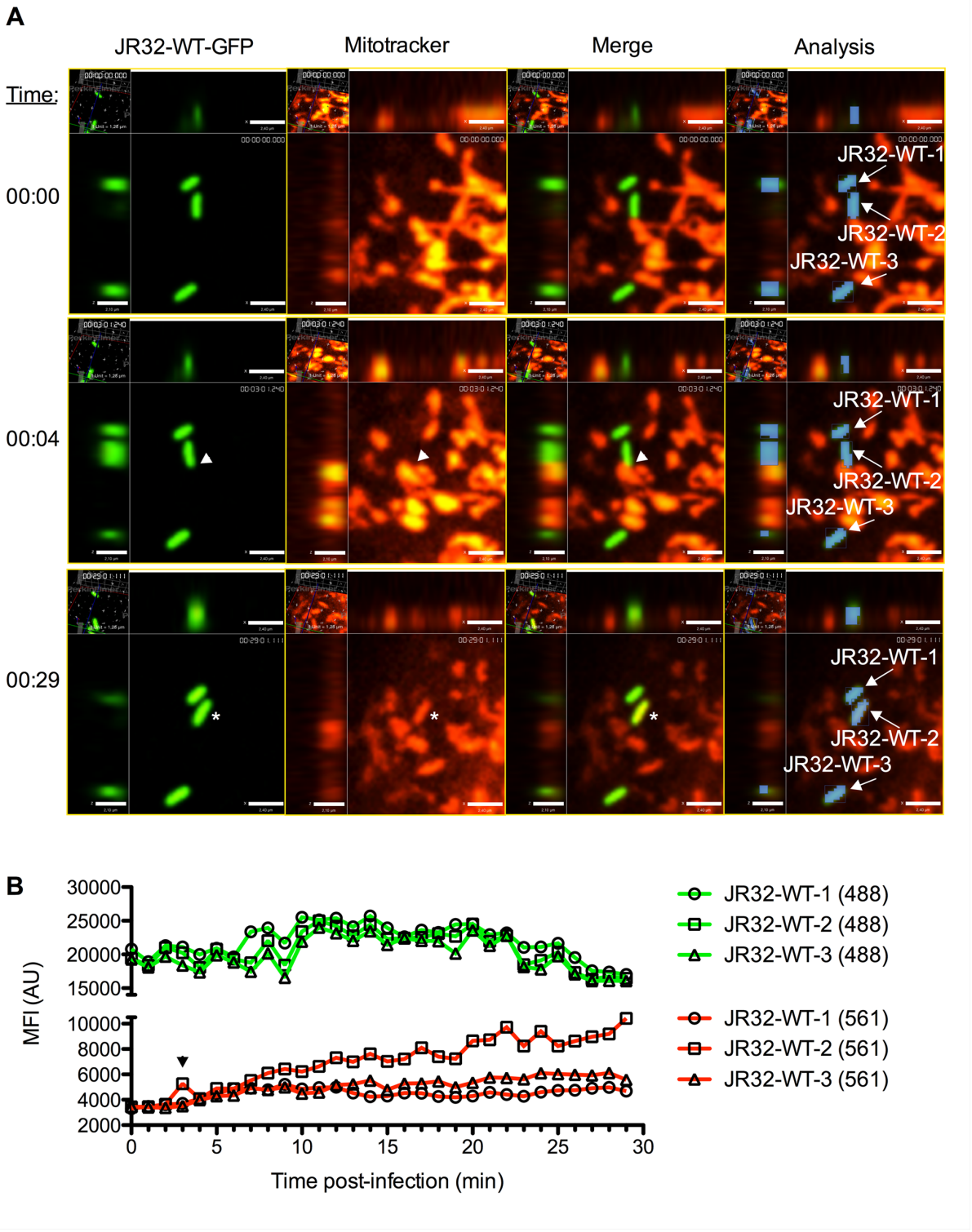
A
JR32-WT-GFP
Mitotracker
Merge
Analysis
Time:
00:00
00:04
00:29
JR32-WT-1
JR32-WT-2
JR32-WT-3
B
MFI (AU)
Time post-infection (min)
JR32-WT-1 (488)
JR32-WT-2 (488)
JR32-WT-3 (488)
JR32-WT-1 (561)
JR32-WT-2 (561)
JR32-WT-3 (561)

Figure S3

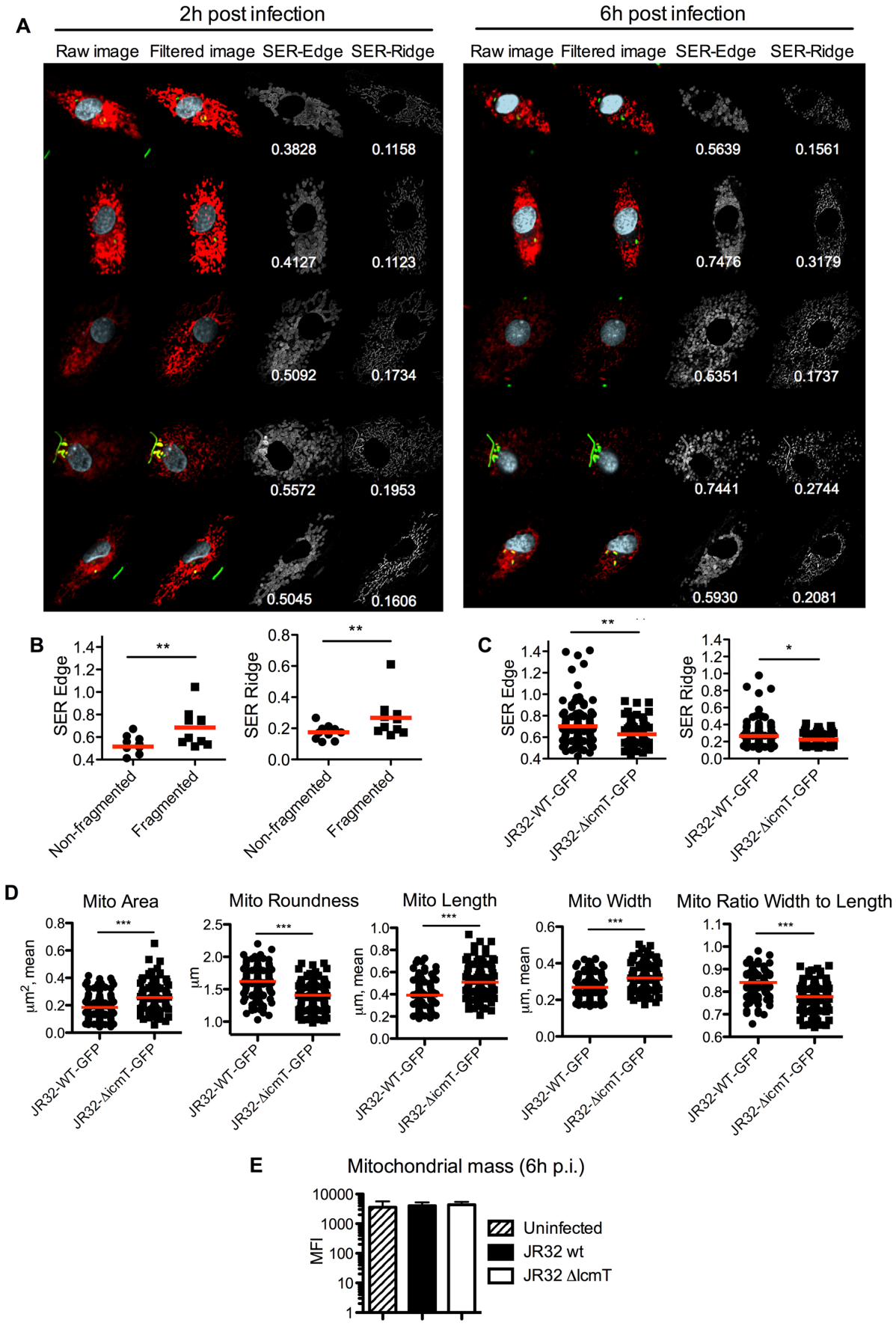
A
2h post infection
6h post infection
Raw image
Filtered image
SER-Edge
SER-Ridge
0.3828
0.1158
0.4127
0.1123
0.5092
0.1734
0.5572
0.1953
0.5045
0.1606
0.5639
0.1561
0.7476
0.3179
0.6351
0.1737
0.7441
0.2744
0.5930
0.2081
B
SER Edge
SER Ridge
Non-fragmented
Fragmented
C
JR32-WT-GFP
JR32-ΔicmT-GFP
D
Mito Area
Mito Roundness
Mito Length
Mito Width
Mito Ratio Width to Length
µm², mean
µm
µm, mean
E
Mitochondrial mass (6h p.i.)
MFI
Uninfected
JR32 wt
JR32 ΔIcmT

Figure S4

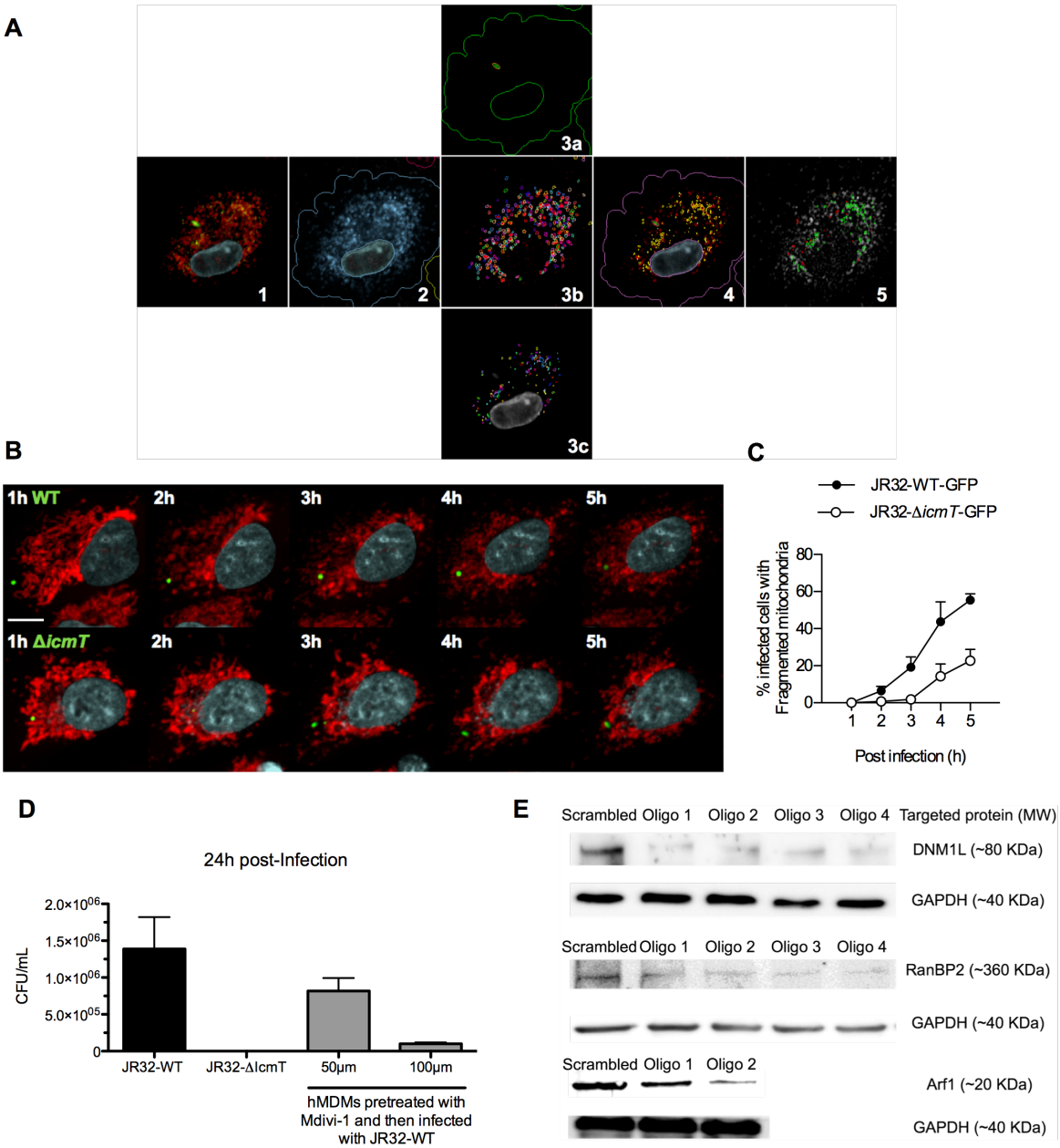
A
3a
1
2
3b
4
5
3c
B
1h WT
2h
3h
4h
5h
1h ΔicmT
2h
3h
4h
5h
C
JR32-WT-GFP
JR32-ΔicmT-GFP
% infected cells with Fragmented mitochondria
80
60
40
20
0
1 2 3 4 5
Post infection (h)
D
24h post-Infection
CFU/mL
2.0×10^06
1.5×10^06
1.0×10^06
5.0×10^05
0
JR32-WT
JR32-ΔIcmT
50μm
100μm
hMDMs pretreated with Mdivi-1 and then infected with JR32-WT
E
Scrambled Oligo 1 Oligo 2 Oligo 3 Oligo 4 Targeted protein (MW)
DNM1L (~80 KDa)
GAPDH (~40 KDa)
Scrambled Oligo 1 Oligo 2 Oligo 3 Oligo 4
RanBP2 (~360 KDa)
GAPDH (~40 KDa)
Scrambled Oligo 1 Oligo 2
Arf1 (~20 KDa)
GAPDH (~40 KDa)
F
Scrambled Mix of 4 Oligos Targeted protein (MW)
DNM1L (~82 KDa)
GAPDH (~38 KDa)
Scrambled Mix of 4 Oligos
Ran (~24 KDa)
GAPDH (~38 KDa)
Scrambled Mix of 4 Oligos
RanBP2 (~358 KDa)
GAPDH (~38 KDa)
G
PI-positive cells [%]
100
80
60
40
20
0
untreated
70% EtOH
Scrambled
DNM1L
RanBP2

Figure S5

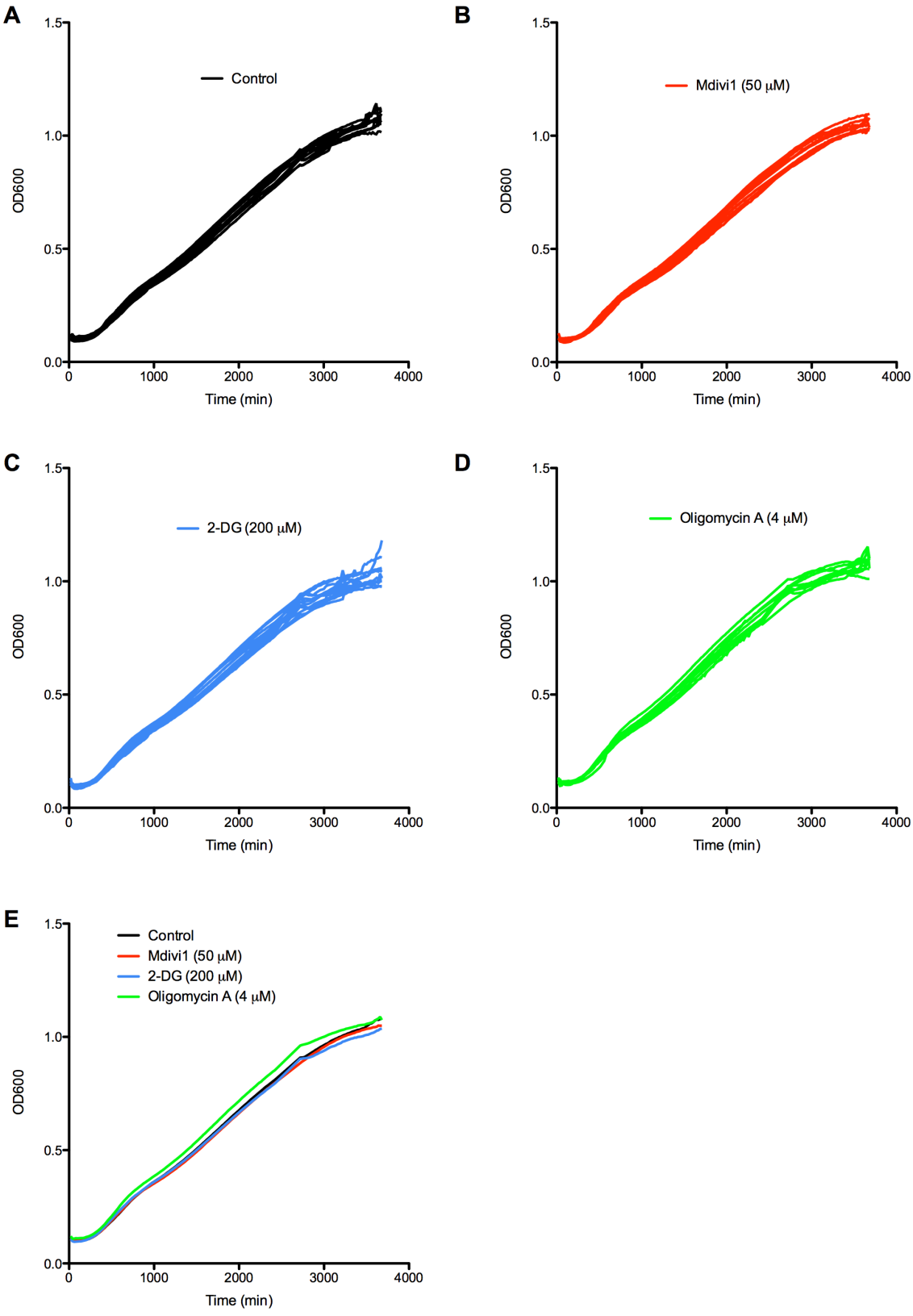
A
Control
OD600
Time (min)
B
Mdivi1 (50 μM)
OD600
Time (min)
C
2-DG (200 μM)
OD600
Time (min)
D
Oligomycin A (4 μM)
OD600
Time (min)
E
Control
Mdivi1 (50 μM)
2-DG (200 μM)
Oligomycin A (4 μM)
OD600
Time (min)

Figure S6

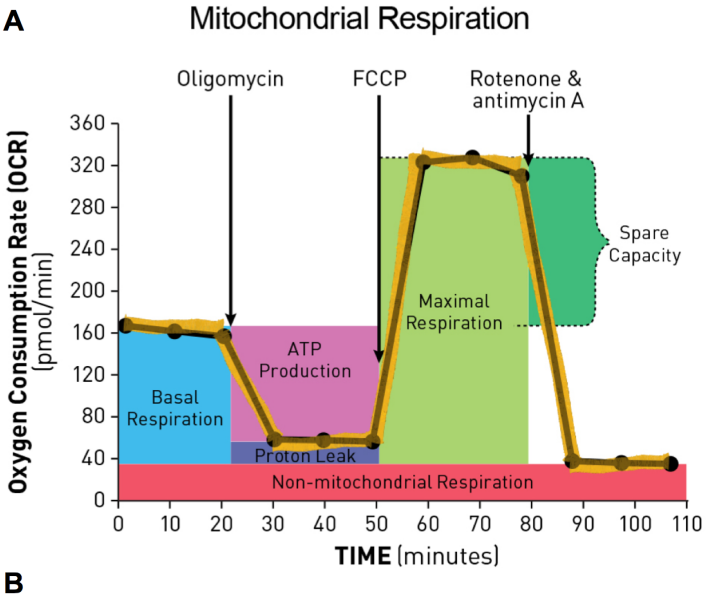

B

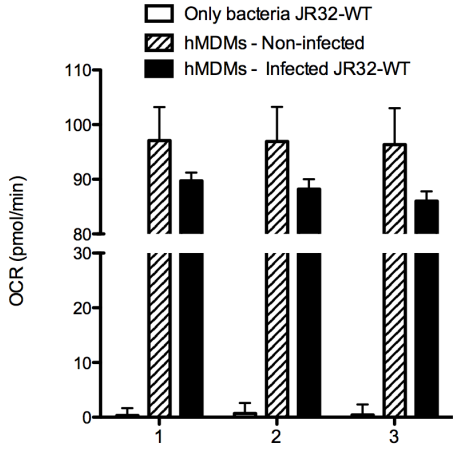

	Only bacteria JR32-WT	hMDMs - Non-infected	hMDMs - Infected JR32-WT
Mean	0.4672	96.79	87.98
Std. Deviation	0.1971	0.3965	1.860

C

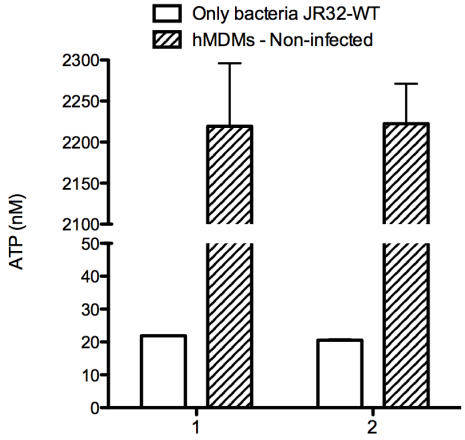

	Only bacteria JR32-WT	hMDMs - Non-infected
Mean	21.20	2221
Std. Deviation	0.9407	2.291